JCB Journal of Cell Biology

ARTICLE

p53 deficiency triggers dysregulation of diverse cellular processes in physiological oxygen

Liz J. Valente[1], Amy Tarangelo[2,5], Albert Mao Li[1], Marwan Naciri[1,3], Nitin Raj[1], Anthony M. Boutelle[1], Yang Li[1], Stephano Spano Mello[1,4], Kathryn Bieging-Rolett[1], Ralph J. DeBerardinis[5,6], Jiangbin Ye[1], Scott J. Dixon[2], and Laura D. Attardi[1,7,8]

The mechanisms by which *TP53*, the most frequently mutated gene in human cancer, suppresses tumorigenesis remain unclear. p53 modulates various cellular processes, such as apoptosis and proliferation, which has led to distinct cellular mechanisms being proposed for p53-mediated tumor suppression in different contexts. Here, we asked whether during tumor suppression p53 might instead regulate a wide range of cellular processes. Analysis of mouse and human oncogene-expressing wild-type and p53-deficient cells in physiological oxygen conditions revealed that p53 loss concurrently impacts numerous distinct cellular processes, including apoptosis, genome stabilization, DNA repair, metabolism, migration, and invasion. Notably, some phenotypes were uncovered only in physiological oxygen. Transcriptomic analysis in this setting highlighted underappreciated functions modulated by p53, including actin dynamics. Collectively, these results suggest that p53 simultaneously governs diverse cellular processes during transformation suppression, an aspect of p53 function that would provide a clear rationale for its frequent inactivation in human cancer.

Introduction

The transcription factor p53 is a critical barrier to the development of cancer, as evidenced by three key observations. First, more than half of all human cancers are associated with direct inactivating mutations in *TP53* (Hollstein et al., 1991; Levine, 2018). Second, Li-Fraumeni patients, who inherit inactivating mutations in *TP53*, are predisposed to early-onset cancers, including breast cancers and sarcomas (Hollstein et al., 1991). Finally, *p53*-null mice succumb to cancer with 100% penetrance (Donehower et al., 1992; Jacks et al., 1994; Kaiser and Attardi, 2018). Intriguingly, despite 40 yr of research on p53, the specific mechanisms by which p53 suppresses tumorigenesis remain incompletely understood.

The best-characterized function of p53 is as a transcription factor. In this role, p53 can elicit widespread transcriptional changes in response to various cellular stresses such as DNA damage, oncogene activation, and hypoxia, to promote specific cellular responses (Mello and Attardi, 2018; Vousden and Prives, 2009). The most studied p53 cellular responses are apoptosis and cell cycle arrest. Apoptosis is triggered by p53 in response to stressors such as acute DNA damage, via transcriptional up-regulation of proapoptotic genes such as the Bcl-2 family members *Puma* and *Noxa*. p53 can also limit cellular proliferation by inducing G_1 or G_2 arrest. For example, at the G_1/S boundary, p53 promotes transient cell cycle arrest in response to genotoxic damage by up-regulating the p21 CDK inhibitor, a measure that is thought to facilitate DNA repair (Karimian et al., 2016). It is through these canonical responses that p53 was proposed to act as a "guardian of the genome," ensuring that upon acquisition of DNA damage, cells would transiently arrest to repair this damage or, alternatively, undergo apoptosis to remove damaged cells from the organism, thereby suppressing oncogenic transformation (Lane, 1992).

Several studies have suggested that p53 suppresses tumorigenesis through responses other than acute DNA damage-induced cell cycle arrest or apoptosis. First, a few reports suggested that the pathological response to acute DNA damage by p53, involving widespread induction of apoptosis, is dispensable for p53-mediated tumor suppression (Christophorou et al., 2006; Efeyan et al., 2007; Hinkal et al., 2009). Expanding on this idea were seminal studies using either knock-in mice bearing alterations to p53 that partially impaired its transcriptional capacity ($p53^{25,26}$ [Brady et al., 2011; Jiang et al., 2011] and $p53^{3KR}$ [Li et al., 2012b]) or gene-targeted mice lacking the canonical p53 target genes *p21*, *Puma*, and *Noxa* (Valente et al., 2013). Cells from these

[1]Division of Radiation and Cancer Biology, Department of Radiation Oncology, Stanford University School of Medicine, Stanford, CA; [2]Department of Biology, Stanford University, Stanford, CA; [3]École Normale Supérieure de Lyon, Université Claude Bernard Lyon I, Université de Lyon, Lyon, France; [4]Department of Biomedical Genetics, University of Rochester Medical Center, Rochester, NY; [5]Children's Medical Center Research Institute, University of Texas Southwestern Medical Center, Dallas, TX; [6]Howard Hughes Medical Institute, University of Texas Southwestern Medical Center, Dallas, TX; [7]Department of Genetics, Stanford University School of Medicine, Stanford, CA; [8]Stanford Cancer Institute, Stanford University School of Medicine, Stanford, CA.

Correspondence to Laura D. Attardi: attardi@stanford.edu.

mice displayed defective p53-dependent induction of apoptosis and cell cycle arrest upon acute DNA damage, but the mice were nonetheless resistant to spontaneously arising tumors (Li et al., 2012b; Valente et al., 2013) and cancer in oncogene-driven mouse cancer models (Brady et al., 2011; Jiang et al., 2011). Together, these studies suggest that processes other than p53 responses to acute DNA damage are critical for tumor suppression or, alternatively, that in the absence of these responses, other processes can compensate to impede tumor development (Mello and Attardi, 2018).

A natural result of this revised view of p53-mediated tumor suppression has been increasing emphasis on understanding noncanonical p53 functions. Specifically, beyond regulating proliferation and apoptosis, p53 has been reported in specific settings to regulate additional cellular processes such as metabolism and stemness (Charni et al., 2017; Kaiser and Attardi, 2018). However, it is unclear whether the ability of p53 to regulate each cellular behavior is context dependent, with a specific p53-regulated process being fundamental for tumor suppression only in a particular tumor type. For example, p53-mediated tumor suppression in large T antigen–driven choroid plexus tumors is associated with oncogene-triggered apoptosis, whereas p53-induced apoptosis and DNA repair programs are critical for the suppression of *Eμ-Myc*–driven B cell lymphomas (Eischen et al., 2001; Garrison et al., 2008; Hemann et al., 2004; Janic et al., 2018; Michalak et al., 2009; Yin et al., 1997). Although tumor suppression has been ascribed to one or two specific p53 cell biological functions in such cancer models, a systematic evaluation of a wide range of p53 functions has not been performed within one specific cellular context. Determining how broadly p53 regulates diverse cellular processes in a particular context is a first step toward understanding the cellular basis of p53-mediated tumor suppression. Indeed, the complexity of the p53 transcriptional program, with alterations in the expression of hundreds of target genes, suggests that p53 might simultaneously regulate a variety of cellular functions during transformation suppression (Andrysik et al., 2017; Fischer, 2019).

Here, we examined to what extent the effects of p53 loss are pleiotropic, using an in vitro oncogene-expressing primary mouse embryonic fibroblast (MEF) model system in which p53 plays a critical role in suppressing transformation. Although transformation suppression by p53 in this setting has been associated predominantly with the induction of apoptosis (Lowe et al., 1993; Soengas et al., 1999), we sought to interrogate the role of p53 in regulating a range of other cell biological functions in this context. Importantly, we performed these experiments in physiological (5%) oxygen tensions to more closely model in vivo conditions. By leveraging a spectrum of assays for different cellular processes, we revealed that p53 regulates an array of diverse cellular processes in this context, several of which were apparent only under physiological oxygen conditions. These findings support the intriguing notion that p53-mediated tumor suppression is a complex coordinated process reliant on modulation of numerous cellular programs.

Results

Establishing a platform to interrogate global p53 functions

To interrogate the capacity of p53 to globally regulate a variety of cellular processes during transformation suppression, we examined *E1A;Hras*^{G12V} oncogene-expressing MEFs, as they provide a tractable model in which different cell biological assays can readily be performed and in which p53 plays a potent role as a transformation suppressor. Moreover, unlike many human cancer cell lines, these are primary, early-passage cells into which oncogenes are retrovirally transduced, and they therefore retain intact p53 signaling pathways. Of note, although previous studies have suggested that transformation suppression in these cells is due to apoptosis in response to cellular stress signals (Lowe et al., 1994; Soengas et al., 1999), we sought to determine whether other cellular processes are also regulated simultaneously by p53. To best model the oxygen tensions that most cells encounter in vivo, which range between 2 to 8% for most cells, we cultured cells in physiological oxygen (5% O_2) rather than the standard atmospheric 21% O_2 conditions.

To establish isogenic WT and p53-deficient cell lines, we generated early-passage MEFs from *H11*^{Cas9} mice, in which Cas9 is constitutively expressed from the *H11* promoter (Chiou et al., 2015). Three independent MEF lines were transduced with E1A- and HRas^{G12V}-expressing retroviruses, and then infected with lentiviruses expressing one of two sgRNAs targeting exon 4 of *Trp53* (sgp53) or a nontargeting control (sgNTC) sgRNA (Fig. 1, A and B; and Fig. S1 A). We thus established a panel of early-passage, isogenic, polyclonal p53 WT (sgNTC) and p53-deficient (sgp53) E1A- and HRas^{G12V}-expressing cell lines (three sgNTC and six sgp53 cell lines). We confirmed p53 deficiency by DNA sequencing of the *p53* locus (Fig. S1 B), immunoblotting and immunofluorescence analyses of p53 protein levels (Fig. 1, C and D; and Fig. S1 C), and Western blot or quantitative RT-PCR (qRT-PCR) analysis of p53 target gene expression (Fig. 1, C and E; and Fig. S1, C and D).

To confirm known p53-dependent phenotypes in this model system, we first assayed transformation suppression using soft agar assays, a robust in vitro surrogate of in vivo tumorigenicity (Lin et al., 1998). In 5% O_2, *E1A;Hras*^{G12V} MEFs targeted with sgp53 exhibited significantly greater cell colony formation than sgNTC controls, confirming that p53 inactivation in these cells enhanced their tumorigenic capacity (Fig. 1, F and G; and Fig. S1 E). We next examined apoptosis in response to two distinct stresses: acute DNA damage and serum starvation. Whereas sgNTC *E1A;Hras*^{G12V} MEFs exhibited significant apoptosis in response to acute DNA damage or serum starvation, sgp53-targeted cells were protected from cell death induced by these stimuli, validating the p53-dependent cell death response to different stressors in *E1A;Hras*^{G12V} MEFs (Fig. 1 H and Fig. S1 F). We next sought to understand which additional p53 downstream pathways might also be regulated during transformation suppression by performing a panel of phenotypic assays examining various cellular processes.

p53 does not dampen cellular proliferation in oncogene-expressing MEFs

The canonical responses of p53 to stress stimuli include not only induction of apoptosis, but also inhibition of cellular proliferation. Although the best-characterized p53 function in this regard is in driving cell cycle arrest or senescence in response to a specific stress signal, p53 can also simply dampen proliferation rates (Tyner et al., 1999). We thus sought to determine whether p53 can regulate oncogene-driven cell proliferation in this

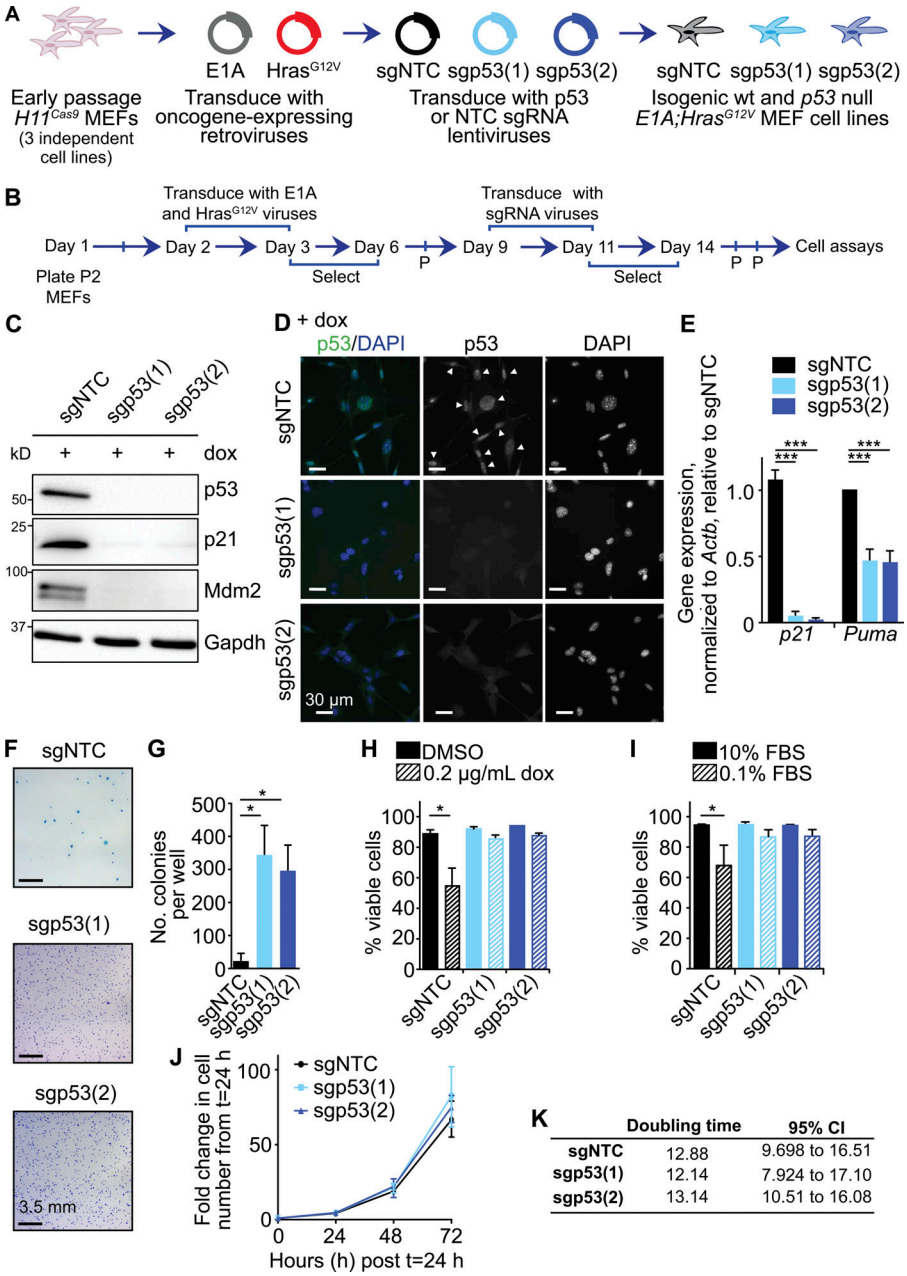

Figure 1. **Generation of WT and *p53*-null *E1A;Hras^{G12V};H11^{Cas9}* MEFs as a platform to dissect p53 function. (A and B)** Schematic illustrating the strategy (A) and chronology (B) for the generation of three isogenic WT (sgNTC) and six p53-deficient (sgp53) *E1A;Hras^{G12V}* MEF lines. **(C)** Immunoblot of p53 and its targets, p21 and Mdm2, after 8-h doxorubicin (dox; 0.2 µg/ml) treatment. *n* = 3 cell lines/sgRNA. Gapdh is a loading control. **(D)** Representative immunofluorescence image of p53 in sgRNA-targeted *E1A;Hras^{G12V}* MEFs treated with 0.2 µg/ml dox for 8 h. DAPI marks nuclei. Scale bar, 30 µm. **(E)** qRT-PCR analysis of p53 target gene expression relative to β-actin in untreated sgRNA-targeted *E1A;Hras^{G12V}* MEFs. *n* = 3 cell lines/sgRNA, in triplicate. Data are mean ± SD; ***, P < 0.0001, two-way ANOVA, Dunnett's multiple comparison test. **(F)** Representative images of soft agar assay of sgRNA-targeted *E1A;Hras^{G12V}* MEFs. Scale bar, 3.5 mm. **(G)** Average colony number ± SD in soft agar assay. *n* = 3 cell lines/sgRNA, in triplicate, three to five independent experiments. *, P < 0.05, one-way ANOVA, Bonferroni's multiple comparison posttest. **(H and I)** Mean viable (AnnexinV/PI-negative) *E1A;Hras^{G12V}* MEFs ± SD after dox treatment (0.2 µg/ml; H) or serum starvation (I) for 24 h. *n* = 3 cell lines/sgRNA, three to five independent experiments. *, P < 0.05, one-way ANOVA, Bonferroni's multiple comparison posttest. **(J)** LUNA cell counter proliferation analysis of sgRNA-targeted *E1A;Hras^{G12V}* MEFs starting 24 h after plating. *n* = 3 cell line/sgRNA. Data are mean fold change in cell number ± SD. **(K)** Doubling time from nonlinear regression analysis of growth curves. CI, confidence interval, *n* = 3 cell lines/sgRNA. For A–K, all experiments were performed in physiological (5%) oxygen.

cellular model. We found no significant difference in the proliferative rate between sgNTC- and sp53-targeted *E1A:Hras^{G12V}*-expressing MEFs (Fig. 1, J and K). Although p53 is classically considered a regulator of the G_1-S transition, expression of E1A in this cellular model inactivates retinoblastoma (Rb) family member-mediated inhibition of cell cycle progression, the primary mechanism by which p53 is thought to inhibit cell proliferation (Deng et al., 2005; Narita et al., 2003). Thus, while p53 is capable of triggering apoptosis in *E1A:Hras^{G12V}*-expressing MEFs, it does not clearly inhibit cell proliferation in this model.

p53 regulates ploidy in *E1A;Hras^{G12V}* MEFs

A hallmark of dysregulated G_1-S progression triggered by p53 deficiency is genomic instability, an observation that earned p53 the title of "guardian of the genome" (Lane, 1992). p53 is thought to preserve genomic integrity by inducing G_1 arrest when cells have sustained DNA damage or have undergone aberrant mitosis with consequent ploidy anomalies, known as the tetraploidy checkpoint (Fujiwara et al., 2005; Ganem et al., 2014; Lanni and Jacks, 1998; Liu et al., 2004). Given the lack of cell cycle phenotype with p53 inactivation in *E1A;Hras^{G12V}* MEFs, we sought to determine whether p53 deficiency still promotes genome destabilization. To this end, we first performed metaphase spreads on cells of each genotype grown in 5% O_2 and quantitated chromosome number (Fig. 2, A–C). Cells targeted with sgp53 exhibited a significantly higher proportion of cells with >40 chromosomes than sgNTC controls, including both tetraploid and polyploid cells (Fig. 2, A–C). To confirm this finding in cells undergoing cell division (not metaphase arrested), we used the FUCCI (fluorescent ubiquitination-based cell cycle indicator)

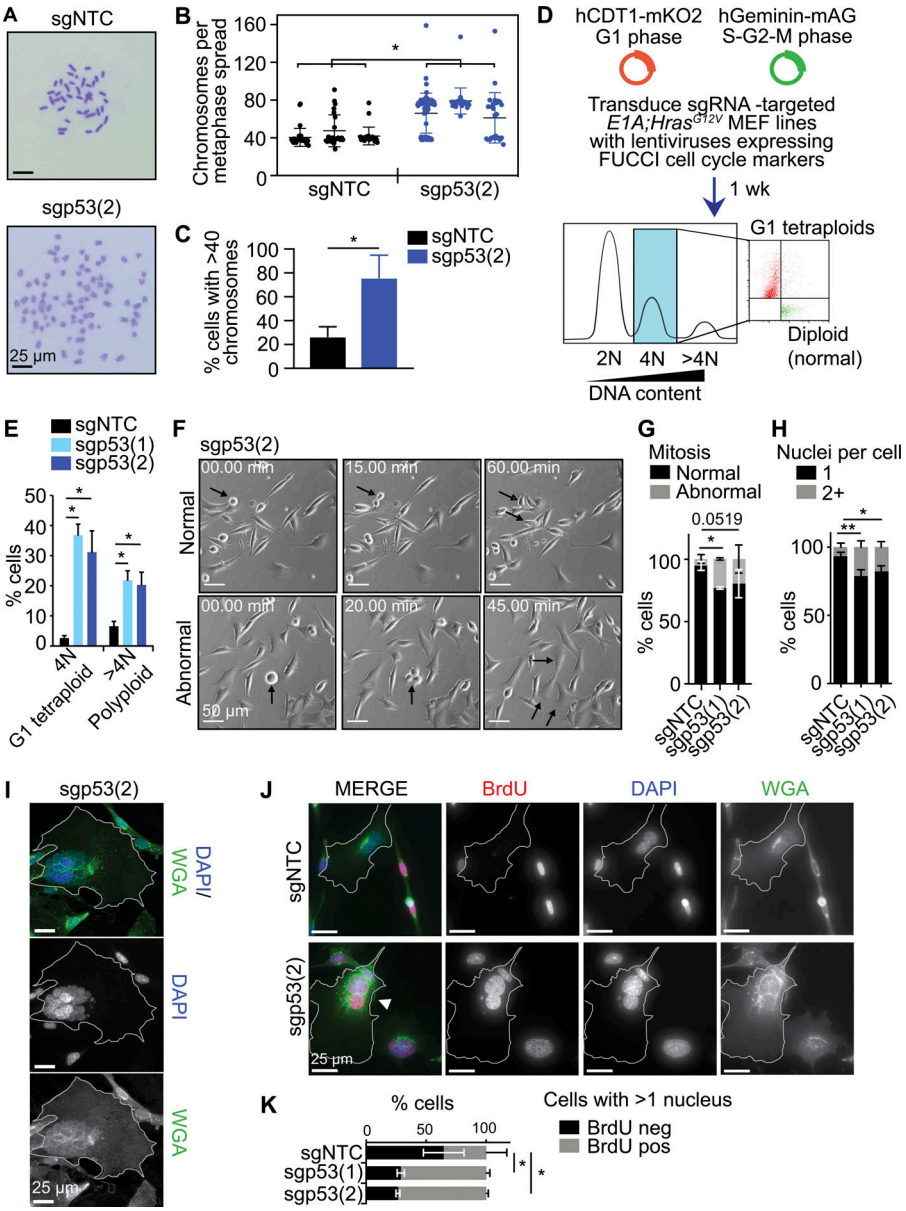

Figure 2. **p53 promotes genomic stability in *E1A;Hras^{G12V};H11^{Cas9}* MEFs. (A)** Representative metaphase spreads from sgNTC and sgp53(2) *E1A;Hras^{G12V}* MEFs. Scale bar, 25 µm. **(B)** Quantitation of chromosomes per cell from metaphase spreads. *n* = 3 cell lines/sgRNA. >30 cells analyzed per cell line. Data are presented as mean ± SD; *, P < 0.05, nested *t* test. **(C)** Percentage of *E1A;Hras^{G12V}* MEFs with >40 chromosomes. Data are mean ± SD, *n* = 3 cell lines/sgRNA. >30 cells analyzed per cell line. *, P < 0.05, Mann–Whitney unpaired *t* test. **(D)** Generation of FUCCI cell cycle marker–expressing variants of *E1A;Hras^{G12V}* MEFs. **(E)** Quantitation of G_1 tetraploid and polyploid populations in sgRNA-targeted *E1A;Hras^{G12V}* MEFs. Data represent the mean ± SD of *n* = 3 cell lines/sgRNA. *, P < 0.05, two-way ANOVA, Dunnett's multiple comparison test. **(F)** Montage of normal and abnormal mitotic events in sgp53(2)-targeted *E1A;Hras^{G12V}* MEFs from time-lapse imaging. Cells of interest are indicated with black arrows. Scale bar, 50 µm. **(G)** Quantitation of abnormal mitotic events in *E1A;Hras^{G12V}* MEFs. *n* = 3 cell lines/sgRNA, with >50 mitotic events analyzed per cell line. Data are mean ± SD; *, P < 0.05, one-way ANOVA, Bonferroni's multiple comparison post-test. **(H)** Nucleus number in *E1A;Hras^{G12V}* MEFs. Data are mean ± SD of *n* = 3 cell lines/sgRNA. *, P < 0.05; **, P < 0.005, two-way ANOVA, Tukey's multiple comparisons test. **(I)** Representative image of a multinucleated sgp53(2)-targeted *E1A;Hras^{G12V}* MEF. WGA marks cell membrane, and DAPI marks nuclei. Scale bar, 25 µm. **(J)** Representative BrdU proliferation analysis of multinucleated sgNTC and sgp53(2) *E1A;Hras^{G12V}* MEFs. White lines indicate outlines of multinucleated cells. White arrows indicate BrdU$^+$ multinucleated cells. Scale bar, 25 µm. **(K)** Quantitation of BrdU-positive multinucleated sgRNA-targeted *E1A;Hras^{G12V}* MEFs. Data are mean ± SD, *n* = 3 cell lines/sgRNA; *, P < 0.05, two-way ANOVA, Dunnett's multiple comparison test. For A–K, all experiments were performed in physiological (5%) oxygen.

cell cycle marker system, which differentially marks cells in G_1 and G_2/M phase (Sakaue-Sawano et al., 2008). Together with DNA content analysis, the proportion of normal diploid cells in G_2/M can be distinguished from abnormal tetraploid cells and polyploid cells in G_1 (Fig. 2 D). We observed a significantly higher percentage of both G_1 tetraploid and polyploid cells in sgp53-targeted MEFs than in sgNTC MEFs, demonstrating that p53 maintains normal ploidy in *E1A;Hras^{G12V}* MEFs, even without regulating proliferation rates (Fig. 2 E).

Next, to investigate the types of abnormal mitotic events in sgp53-targeted cells that might drive altered ploidy, we performed time-lapse, live-cell imaging analysis of mitosis. *E1A;Hras^{G12V}* sgp53-targeted MEFs exhibited an increased proportion of abnormal mitotic events (defined here as multipolar spindle formation or failed cytokinesis) relative to sgNTC cells (Video 1 and Fig. 2, F and G). One outcome arising from these mitotic defects is the generation of cells with more than one nucleus (Fig. 2 H). Specifically, while any cell with more than one nucleus in sgNTC MEFs tended to be only binucleate, p53-deficient cells exhibited both binucleate and multinucleated cells, with a small proportion of these multinucleated cells displaying >10 apparent nuclei (Fig. 2 I). Interestingly, after pulsing with BrdU, ~70% of these p53-deficient bi- and multinucleate cells displayed BrdU positivity, compared with only ~40% of the binucleate cells in sgNTC cells (Fig. 2, J and K). This finding suggests that in the absence of p53, these highly abnormal cells are more likely to attempt to continually divide, supporting the idea of a failed tetraploidy checkpoint in these cells. Together, these results demonstrate that, despite being unable to dampen proliferation, p53 remains capable of regulating mitotic fidelity in *E1A;Hras^{G12V}* MEFs, perhaps by direct regulation of mitotic events and/or clearance of cells that have undergone abnormal mitosis. These studies thus underscore the importance of p53 in faithful genome propagation.

p53 promotes DNA repair in response to acute DNA damage in *E1A;Hras^{G12V}* MEFs

Beyond maintaining genomic integrity by regulating ploidy, p53 has also been shown to promote different types of DNA repair (Williams and Schumacher, 2016). Interestingly, the capacity of p53 to regulate DNA repair has recently been suggested to be critical for p53-mediated tumor suppression in lymphoid cells (Janic et al., 2018; Valente et al., 2013). To determine whether p53 function in *E1A;Hras^{G12V}* MEFs is also linked to the repair of damaged DNA, we harvested WT and p53-deficient *E1A;Hras^{G12V}* MEFs at various time points after treatment with 2 Gy γ-irradiation (IR) and immunostained cells with γH2AX antibodies to detect foci that form at sites of double-strand breaks (Fig. 3 A). We found no significant difference in the percentages of cells exhibiting high nuclear γH2AX fluorescence in either the basal state or the early response to acute DNA damage (1 h after IR) in cells with different p53 statuses. In contrast, sgp53-targeted *E1A;Hras^{G12V}* MEFs exhibited significantly higher γH2AX staining 6 h after IR than sgNTC cells, suggesting delayed induction of DNA repair (Fig. 3, B and C). Both sgNTC- and sgp53-targeted cells showed little evidence of cell death 6 h after IR (not depicted), suggesting that differences in γH2AX levels did not arise from differences in apoptosis after irradiation. By 24 h after IR, γH2AX levels in both sgNTC- and sgp53-targeted MEFs returned to baseline levels (Fig. 3, B and C), indicating that factors other than p53 may contribute to late DNA repair responses. These results indicate that p53 plays a critical role in enhancing early DNA repair responses to acute DNA damage in *E1A;Hras^{G12V}* MEFs.

p53 loss does not significantly impact induction of ferroptosis in *E1A;HRas^{G12V}* MEFs

Recently, the ability of p53 to promote ferroptosis, an iron-dependent form of cell death that culminates in toxic lipid peroxidation, has been suggested to be critical for p53-mediated tumor suppression (Jiang et al., 2015b). Ferroptosis can be induced by inhibiting cystine import via the cystine/glutamate antiporter system x_c^- using the small molecule erastin2 and can be blocked by small-molecule inhibitors of lipid peroxidation, such as ferrostatin-1 (Dixon et al., 2012). We examined whether p53 deficiency in *E1A;Hras^{G12V}* MEFs altered sensitivity to erastin2-induced ferroptosis. Initially, we performed FACS-based cell viability assays in 5% O_2, to determine the sensitivity of these cells to erastin2-induced ferroptosis. After 16 h of treatment, sgNTC *E1A;Hras^{G12V}* MEFs exhibited decreased viability relative to sgp53-targeted cells (Fig. 4 A). However, while cotreatment of cells with ferrostatin-1 reduced erastin2-induced lipid peroxidation, it failed to rescue erastin2-induced cell death in sgNTC cells (Fig. 4 A). These findings suggest that erastin2 induces nonferroptotic cell death in *E1A;Hras^{G12V}* MEFs in 5% O_2.

To further probe the role of p53 in ferroptosis, we shifted our studies to atmospheric (21%) O_2, under which erastin2-induced ferroptosis has been well characterized. We monitored ferroptosis in erastin2-treated *E1A;Hras^{G12V}* MEFs expressing the nuclear-localized mKate2 live-cell marker and incubated with the dead cell marker SYTOX Green (Fig. 4 B). Erastin2 induced robust cell death in a dose-dependent manner in both sgNTC- and sgp53-targeted *E1A;Hras^{G12V}* MEFs (Fig. 4, C and D), and cell death was rescued by cotreatment with ferrostatin-1, consistent with the induction of ferroptosis (Fig. 4 E). Upon comparing the dose–response curves over time (Fig. 4 F), and EC_{50} values (Fig. 4 G), no significant difference was observed between sgp53 and sgNTC cells, suggesting that p53 does not regulate sensitivity to erastin2-induced ferroptosis in *E1A;Hras^{G12V}* MEFs.

To probe why *E1A;Hras^{G12V}* MEFs grown in 5% O_2 displayed different sensitivity to erastin2-induced ferroptosis from that of cells cultured in 21% O_2, we analyzed basal lipid peroxidation. Interestingly, both p53-expressing and p53-deficient cells in 5% O_2 exhibited less basal lipid peroxidation than in 21% O_2 (Fig. 4 H). Thus, lower basal peroxidation in 5% O_2 may present a barrier for the induction of ferroptosis, leading cells to engage another cell death pathway upon cystine deprivation, a notion consistent with erastin2 triggering apoptosis in some conditions where ferroptosis is blocked (Huang et al., 2018a; Huo et al., 2016). These findings also underscore the importance of examining cellular phenotypes in physiological oxygen conditions.

p53 restrains glycolysis and regulates nucleotide metabolism in *E1A;Hras^{G12V}* MEFs

The capacity of p53 to inhibit the Warburg effect, by dampening glycolysis and promoting oxidative phosphorylation, has been proposed as a mechanism by which p53 suppresses cellular transformation (Vousden and Ryan, 2009). Most studies investigating the role of p53 in metabolism have been performed in atmospheric 21% O_2, whereas oxygen availability in vivo ranges between 2% and 8% O_2 for most cells. Given our findings highlighting the importance of oxygen tension for the induction of ferroptosis, we sought to determine the role of p53 in metabolic regulation in both atmospheric and physiological oxygen tensions.

To examine the role of p53 in glucose metabolism in *E1A;Hras^{G12V}* MEFs, we performed [U-^{13}C]–glucose tracing experiments in either 5% or 21% O_2 followed by liquid chromatography (LC)/mass spectrometry (MS) to determine labeled metabolite levels (Fig. 5 A). In 5% O_2, sgNTC *E1A;Hras^{G12V}* MEFs displayed enhanced glycolysis and decreased TCA cycle activity relative to sgNTC cells grown in 21% O_2, with significantly higher abundance of total and ^{13}C-labeled lactate (Fig. 5 B), decreased percentage of (m+2) ion abundance for several TCA intermediates like fumarate and malate (Fig. 5 C), and lower (m+2) citrate:(m+3) lactate ion ratios (Fig. 5, D and E; sgNTC [5%] versus sgNTC [21%]; $P < 0.05$), indicating a relative suppression of pyruvate oxidation at 5% O_2. Notably, p53 was able to enhance pyruvate oxidation to produce citrate in 5% O_2, evidenced by a significantly higher (m+2) citrate:(m+3) lactate ratio in sgNTC cells than in sgp53(2) cells, whereas p53-dependent differences in 21% O_2 were not significant (Fig. 5, D and E). Together, these findings suggest that p53 demonstrates a more pronounced regulatory role in pyruvate oxidation and tumor cell metabolism in physiological oxygen and highlights the importance of using appropriate oxygen tensions during cell culture in vitro to accurately model in vivo cellular function.

The effects of p53 on cellular metabolism extend beyond glycolysis and oxidative phosphorylation (Vousden and Ryan,

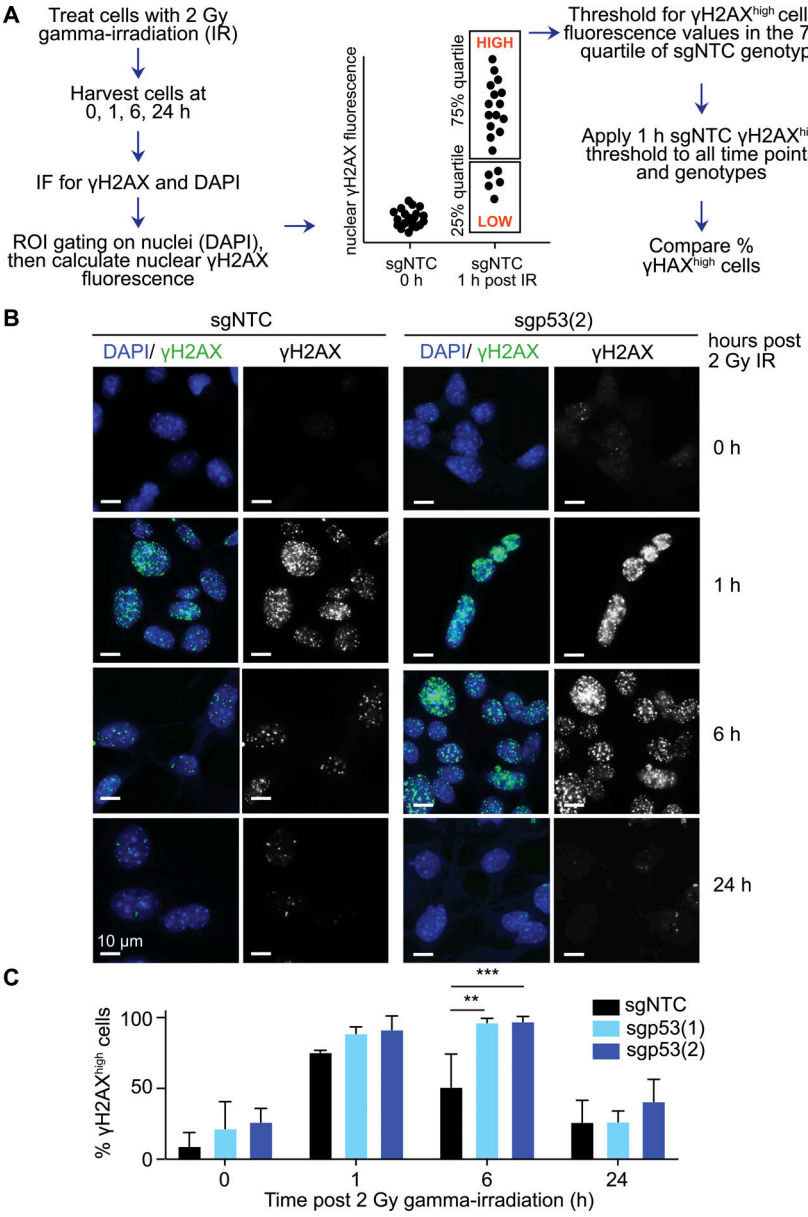

Figure 3. **p53 promotes DNA repair in response to acute DNA damage in *E1A;Hras^{G12V};H11^{Cas9}* MEFs.** **(A)** Schematic of the γIR of *E1A;Hras^{G12V}* MEFs and subsequent analysis of DNA repair over time. **(B)** Representative images of γH2AX foci in *E1A;Hras^{G12V}* MEFs at different times after IR. DAPI marks nuclei. Scale bar, 10 µm. **(C)** Average percentage of γH2AX^{high} cells ± SD, n = 3 cell lines/sgRNA with 40–105 cells analyzed per cell line/time point. **, P < 0.005; ***, P < 0.0005, two-way ANOVA, Dunnett's multiple comparison test. For A–C, all experiments were performed in physiological (5%) oxygen.

2009). To gain a more comprehensive view of how p53 modulates metabolism in 5% O_2, we performed targeted LC-MS/MS metabolomics analysis on sgNTC- and sgp53-targeted *E1A;Hras^{G12V}* MEFs (Fig. 5 F) and identified 15 metabolites with significantly different abundances between genotypes (Fig. 5 G and Table S1). Metabolite set enrichment analysis of metabolites with abundance changes of at least twofold upon p53 loss indicated a strong nucleotide signature, involving both purine- and pyrimidine-related metabolites (Fig. 5, G and H). Notably, in addition to decreased nucleoside/tide levels, sgp53-targeted cells exhibited significant increases in levels of glutamine and glycine, both of which are precursors for nucleotide metabolism but are also involved in other metabolic pathways such as serine and one-carbon metabolism (Fig. 5 G). Collectively, these results confirm that p53 restrains alterations in glucose metabolism typical of the Warburg effect, primarily through a rebalancing of glycolytic and oxidative metabolism. Moreover, p53 influences other aspects of metabolism, such as nucleotide availability, in *E1A;Hras^{G12V}* MEFs.

p53 restrains migration and invasion in *E1A;Hras^{G12V}* MEFs

Although roles for p53 in inducing apoptosis, maintaining genomic stability, and regulating metabolism may be central for restraining initial tumor growth, p53 may also modulate tumor progression. The ability of WT p53 to modulate behaviors paramount for metastasis, including migration and invasion, has been shown only in limited contexts (Gadea et al., 2007; Muller et al., 2011). Interestingly, in live-cell imaging experiments of *E1A;Hras^{G12V}* MEFs grown in 5% O_2 (Fig. 2 F), we observed that sgp53-targeted cells exhibit more pronounced lamellipodia (membrane protrusions at the leading edges of motile cells thought to be critical for driving cellular migration) than sgNTC cells (Video 2; Krause and Gautreau, 2014). Hence, we analyzed cellular migration by performing Boyden chamber Transwell

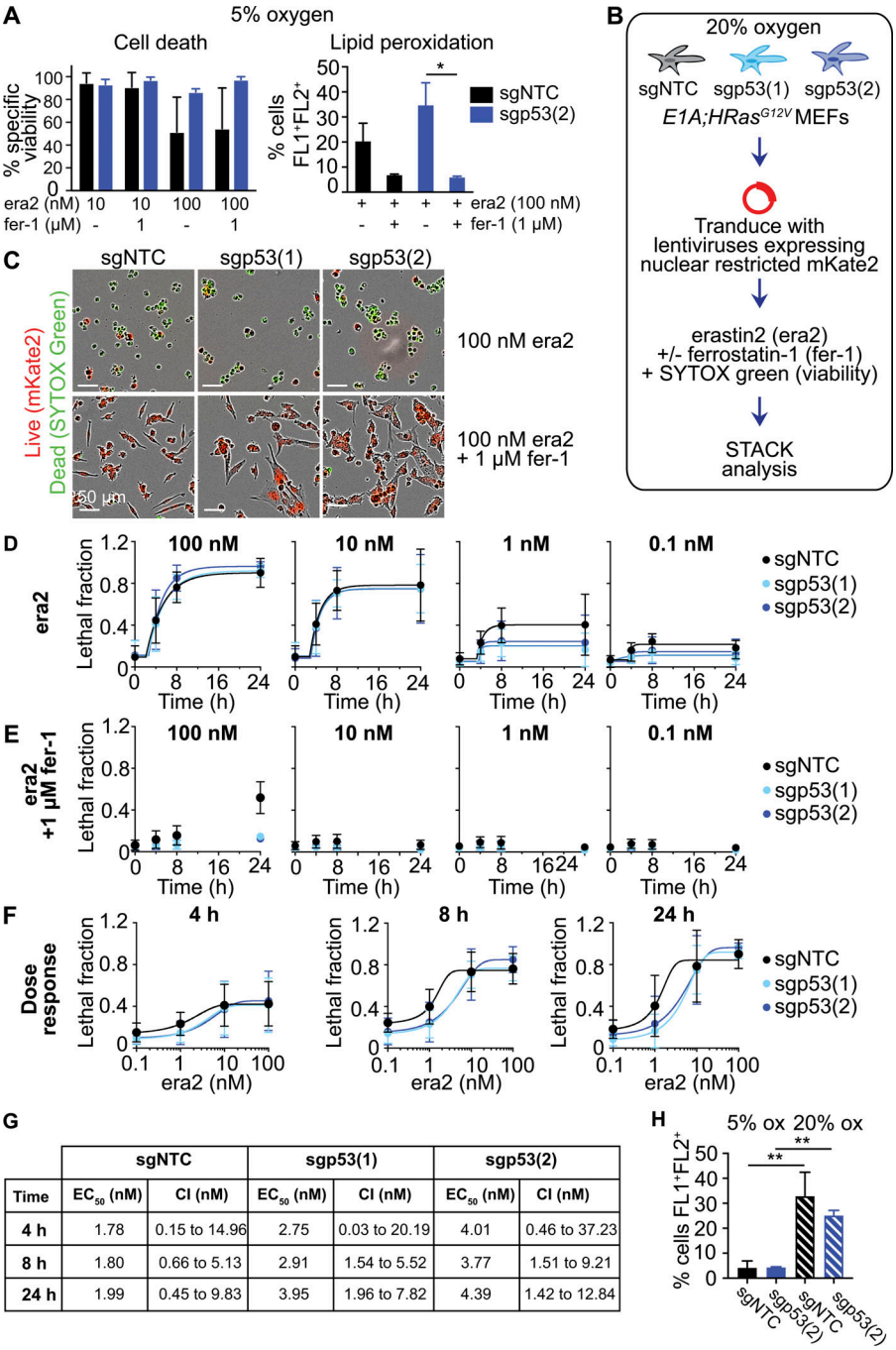

	sgNTC		sgp53(1)		sgp53(2)	
Time	EC_{50} (nM)	CI (nM)	EC_{50} (nM)	CI (nM)	EC_{50} (nM)	CI (nM)
4 h	1.78	0.15 to 14.96	2.75	0.03 to 20.19	4.01	0.46 to 37.23
8 h	1.80	0.66 to 5.13	2.91	1.54 to 5.52	3.77	1.51 to 9.21
24 h	1.99	0.45 to 9.83	3.95	1.96 to 7.82	4.39	1.42 to 12.84

Figure 4. **p53 does not significantly impact the induction of ferroptosis in *E1A;HRas^{G12V};H11^{Cas9}* MEFs. (A)** PI cell viability and lipid peroxidation analysis on *E1A;Hras^{G12V}* MEFs treated with erastin2 (era2) ± ferrostatin-1 (fer-1) in 5% O_2. *n* = 2 cell lines/sgRNA. Viability data are mean ± SD; *, P < 0.05, one-way ANOVA, Bonferroni's multiple comparison test. Peroxidation data are mean percent $FL1^+FL2^+$ cells ± SD in 2–3 cell lines/sgRNA. *, P < 0.05, Student's *t* test. **(B)** Experimental workflow for ferroptosis assays in 21% O_2. **(C)** Representative IncuCyte images of *E1A;Hras^{G12V}* MEFs in 21% O_2 treated for 8 h with era2 ± fer-1. Live cells are in red, and dead cells are in green. Scale bar, 50 μm. **(D and E)** Cell death in response to era2 (D) or era2 and 1 μM fer-1 (E) in 21% O_2. **(F)** Dose–response curves of era2-treated sgRNA-targeted *E1A;Hras^{G12V};H11^{Cas9}* MEFs at different time points in 21% O_2. **(G)** EC_{50} and confidence interval (CI) values for era2-treated *E1A;Hras^{G12V}* MEFs in 21% O_2. **(H)** Basal lipid peroxidation in 5% and 21% O_2. Data are the mean percentage of $FL1^+FL2^+$ cells ± SD of 3 cell lines/sgRNA; **, P < 0.05, Student's *t* test. For D–G, data are mean ± SD of 3 cell lines/sgRNA in three independent replicates. For EC_{50} doses, the dose parameter was log transformed, and the data were fitted with a sigmoidal four-point curve with Hill slope constrained to 1 using Prism 7 (GraphPad).

assays on sgNTC- and sgp53-targeted cells grown in 5% O_2. Although both sgNTC- and sgp53-targeted *E1A;Hras^{G12V}* MEFs migrated through the Transwell filter, sgp53-targeted cells exhibited approximately threefold greater migration than sgNTC cells over 24 h (Fig. 6, A and B). Notably, these experiments were performed without any growth factor or nutrient gradient, suggesting that even without a specific cue, WT p53 restrained cellular migration in this context. In contrast, while a similar trend was observed in cells cultured in 21% O_2, differences between sgNTC- and sgp53-targeted cell migration were not significant (see Fig. S2 A, no nutrient gradient), suggesting that the capacity of p53 to regulate migration is dampened under atmospheric oxygen conditions.

Next, we sought to determine whether WT p53 also modulates invasiveness in this model system. We performed 3D-collagen matrix invasion assays on sgNTC- and sgp53-targeted cells grown in 5% and 21% O_2. In 5% O_2, both sgNTC- and sgp53-targeted cells formed small colonies within the collagen matrix. However, while sgNTC cells remained as small spheroids, sgp53-targeted cells penetrated into the surrounding collagen matrix, forming star-like, invasive structures (Fig. 6 C). Quantitation of invading colonies indicated there was a dramatic increase in the invasive capacity of sgp53-targeted cells (~70% invasive colonies) relative to sgNTC cells (<5% invasive colonies; Fig. 6 D). Together, these results demonstrate that WT p53 plays a critical role in dampening both the migratory and invasive potential of

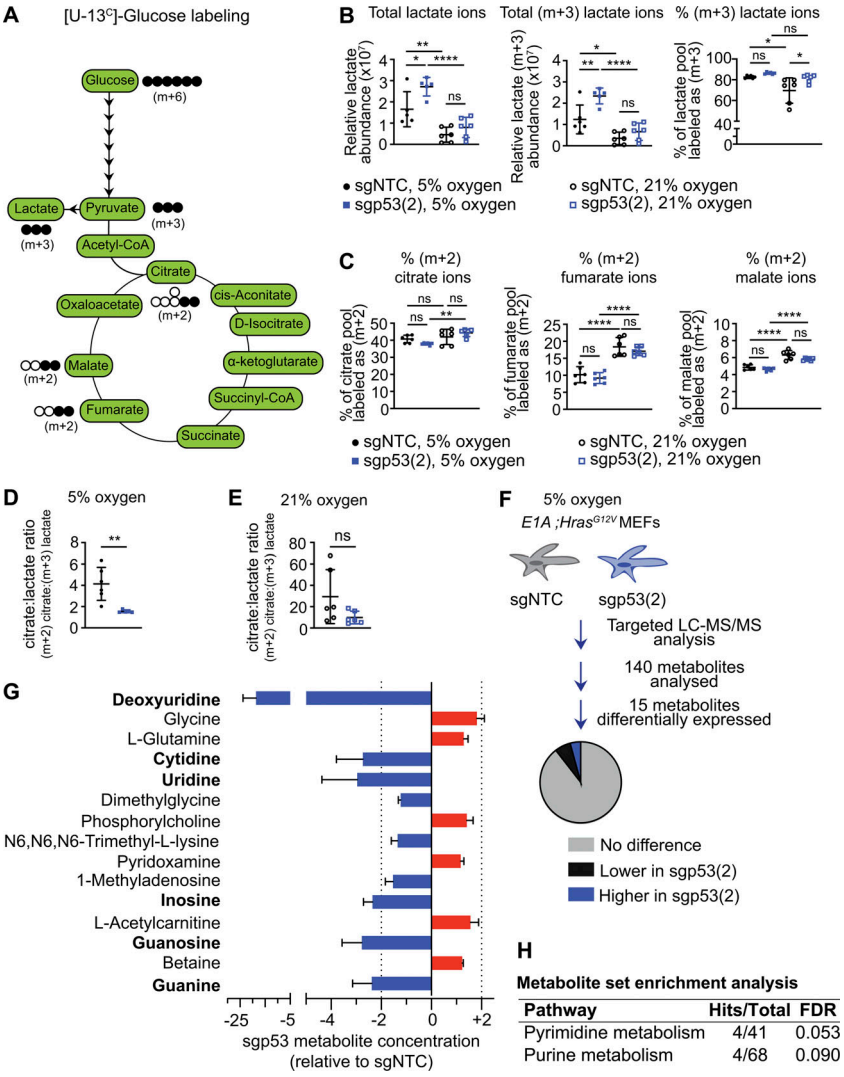

Figure 5. **p53 restrains glycolysis and regulates nucleotide metabolism in *E1A;Hras*^{G12V} MEFs. (A)** Schematic representing the flow of glucose-derived carbon through glycolysis and the TCA cycle. Circles indicate carbon molecules present in each metabolite, and filled-in circles (black) represent glucose-derived carbons. **(B and C)** [U-^{13}C]glucose tracing on sgNTC and sgp53(2) *E1A;Hras*^{G12V} MEFs in 5% and 21% O_2 showing glycolytic (B) and TCA cycle (C) intermediates. Data are mean ± SD of $n = 3$ cell lines/sgRNA, two independent samples/genotype *, $P < 0.05$; **, $P > 0.005$; ****, $P < 0.0001$; ns, not significant ($P > 0.05$), one-way ANOVA, Tukey's multiple comparison test. **(D and E)** (m+2) citrate:(m+3) lactate ion ratio of sgNTC and sgp53(2) *E1A;Hras*^{G12V} MEFs cells in 5% (D) or 21% (E) O_2. Note different axes. Data represent mean ± SD of $n = 3$ cell lines/sgRNA, two independent samples/cell line; **, $P < 0.005$; ns, nonsignificant by Student's t test. $P < 0.05$ for sgNTC (5% O_2) versus sgNTC (21% O_2), one-way ANOVA, Sidak's multiple comparison test. **(F)** Schematic of LC-MS/MS analysis of sgNTC and sgp53(2)-targeted *E1A;Hras*^{G12V} MEFs in 5% O_2. Student's t test ($P < 0.05$). $n = 3$ cell lines/sgRNA. **(G)** Differentially abundant metabolites and the fold change difference of concentration in sgp53(2)-targeted cells relative to sgNTC-targeted cells. Student's t test ($P < 0.05$). $n = 3$ cell lines/sgRNA. **(H)** Pathway enrichment analysis of metabolites exhibiting a more than twofold difference in concentration between sgNTC and sgp53(2)-targeted *E1A;Hras*^{G12V} MEFs. FDR, false discovery rate.

E1A;Hras^{G12V} MEFs in physiological oxygen conditions. In striking contrast, p53-deficient cells grown in 21% O_2 failed to display any invasive behavior (Fig. 6, E and F), again reinforcing the need for appropriate oxygen tensions during cell culture to accurately model p53 function in vitro. Collectively, our results demonstrate that p53 deficiency in neoplastic cells can cause pleiotropic dysregulation of a variety of cellular processes.

The effect of oxygen tension on classic p53-dependent phenotypes

Although the ability of p53 activity to regulate metabolism and invasion was markedly different in 5% and 21% O_2, it remained unclear whether classic p53 pathways were similarly impacted by altering oxygen tension. We therefore performed apoptosis and proliferation assays on *E1A;Hras*^{G12V} MEFs cultured in 5% or 21% O_2. We found that apoptosis induced by acute DNA damage and serum deprivation was similar in magnitude and p53 dependence in both 5% and 21% O_2 (Fig. S2 B). In contrast, whereas proliferation was accelerated in physiological conditions, p53 loss had no significant impact in either oxygen tension (Fig. S2 C). Thus, the consequences of altering oxygen tension are phenotype specific, with p53-dependent noncanonical responses appearing more affected. It also remained unclear how oxygen tension might affect tumorigenicity in vitro. To address this question, we assessed the impact of altering environmental oxygen on tumorigenic potential using soft agar assays. Although sgp53(2) cells formed significantly more colonies than sgNTC cells in both 5% and 21% O_2 (Fig. S2, D and E), sgp53(2) cells grown in 21% O_2 formed fewer colonies than cells in 5% O_2. Thus, p53-deficient *E1A;Hras*^{G12V} MEFs grown in 5% O_2 are significantly more tumorigenic than the same cells grown in 21% O_2, suggesting that studies performed under atmospheric oxygen conditions may underestimate the contribution of p53 action in transformation suppression. Together, these findings further highlight the need for use of appropriate oxygen tension during cell culture in vitro to accurately model in vivo cellular function.

p53 deficiency induces pleiotropic alterations in HCT116 human colon carcinoma cells

As our studies clearly suggested that p53 deficiency drives pleiotropic changes in cell behavior in *E1A;Hras*^{G12V} MEFs, we next sought to determine if such pleiotropy is observed in other cellular contexts. We thus examined a set of canonical and

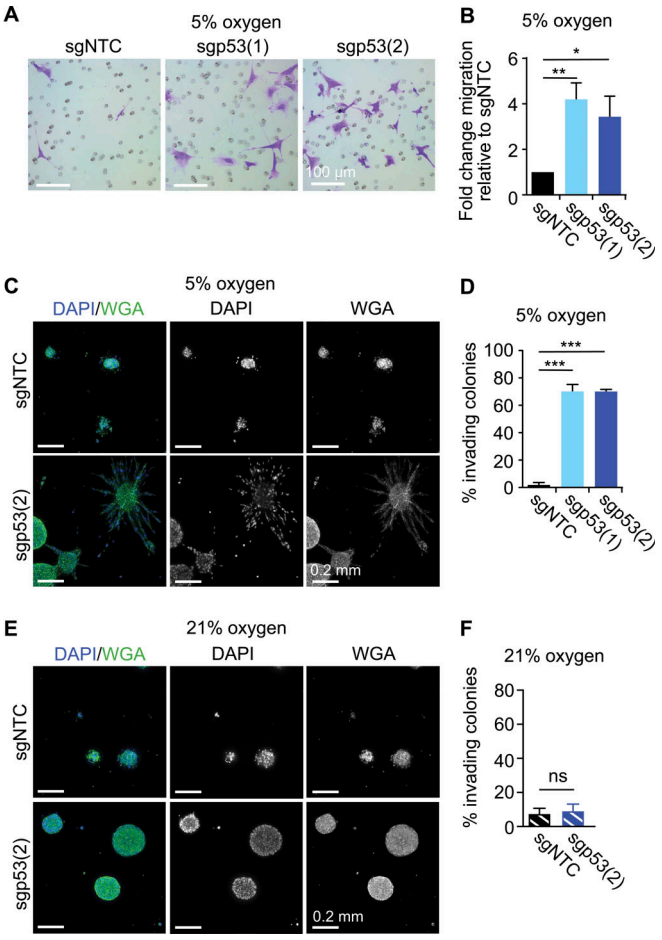

Figure 6. **p53 inhibits migration and invasion of *E1A;Hras^{G12V};H11^{Cas9}* MEFs. (A)** Representative bright-field images of sgRNA-targeted *E1A;Hras^{G12V}* MEFs migrating through Boyden chamber filter and stained with Giemsa. Scale bar, 100 µm. **(B)** Mean fold change in migrating *E1A;Hras^{G12V}* MEFs ± SD, expressed relative to counterpart sgNTC control cell line. *n* = 3 cell lines/sgRNA; *, P < 0.05 **, P < 0.005, one-way ANOVA, Bonferroni's multiple comparisons test. **(C and E)** Representative images of sgNTC and sgp53(2) *E1A;Hras^{G12V};H11^{Cas9}* cultured in a 3D-collagen matrix in 5% (C) or 21% (E) O_2. WGA marks cell membranes, and DAPI marks nuclei. Scale bar, 0.2 mm. **(D)** Percentage invading colonies in 5% O_2. Data are mean ± SD, *n* = 3 cell lines/sgRNA; ***, P < 0.0001, one-way ANOVA, Bonferroni's multiple comparisons test. **(F)** Percentage invading colonies in 21% O_2. Data are mean ± SD, *n* = 3 cell lines/sgRNA; ns, not significant (P > 0.05), Mann–Whitney unpaired *t* test.

noncanonical phenotypes in isogenic WT and p53-deficient cells in another model under 5% O_2 conditions. We used the human HCT116 colon carcinoma cell line, with the dual purpose of examining p53 action in a carcinoma context as well as in human cells (Bunz et al., 1998). We found first that HCT116 cells lacking p53 underwent significantly less apoptosis in response to serum starvation, but not DNA damage (Fig. S3 A) than p53-proficient HCT116 cells. As in the *E1A;Hras^{G12V}* MEFs (Fig. 1 J), *TP53* deletion did not significantly impact the proliferative rate of HCT116 cells (Fig. S3 B). We then assessed p53 noncanonical functions and observed that *TP53* deletion significantly increased the number of polyploid HCT116 cells relative to *TP53*-proficient HCT116 cells (Fig. S3 C). Moreover, in [U-^{13}C] glucose tracing experiments, HCT116 cells lacking p53 exhibited increased abundance of total and labeled pools of the glycolytic intermediates glucose-6-phosphate and phosphoenolpyruvate (Fig. S3 D), suggesting an induction of glycolysis upon *TP53* loss. Interestingly, *TP53*-deficient cells had lower lactate ion counts (Fig. S3 D), higher total and (m+2) ion counts of early TCA cycle intermediates (Fig. S3 E), and an increased (m+2) citrate:(m+3) lactate ion ratio (Fig. S3 F) relative to *TP53*-proficient cells, all suggestive of increased pyruvate oxidation. This is surprising given the described role for p53 in promoting oxidative respiration and could suggest that under physiological oxygen conditions, p53 inhibits TCA cycle activity in this setting. Finally, we assessed the impact of p53 loss on the invasive capacity of HCT116 cells and observed that *TP53* loss promoted a small but nonsignificant increase in the percentage of invading colonies in 3D-collagen matrix assays (Fig. S3, G and H). Together, these findings demonstrate that *TP53* deficiency in HCT116 cells promotes multiple alterations in cell behavior, supporting the idea that pleiotropy of p53 action is conserved in carcinomas and in human cells.

p53 induces diverse transcriptional programs under physiological oxygen conditions

Collectively, our findings demonstrate an expansive role for p53 in regulating varied cellular processes in oncogene-expressing cells under physiological oxygen conditions (Fig. 7 A). To develop a broader understanding of the cellular pathways transcriptionally regulated by p53 in this setting, we performed gene expression analysis on early-passage sgNTC- and sgp53-targeted *E1A;Hras^{G12V}* MEFs grown in 5% O_2 (Fig. 7 B). RNA sequencing (RNA-seq) analysis revealed that p53 elicits widespread transcriptional changes in *E1A;Hras^{G12V}* MEFs, with 2,520 genes differentially expressed between sgNTC- and sgp53-targeted cells (Fig. 7, B and C; and Table S2). Given that our RNA-seq dataset was generated in 5% O_2, while most studies on p53 have been performed at 21% O_2, we first sought to determine how well our dataset aligned with the classic p53 transcriptional program (Fig. 7 D). We indeed observed a strong p53 dependence for classic p53 target genes, such as *Cdkn1a*, *Bax*, and *Mdm2*.

Next, we sought to determine if our dataset could provide new insight into how p53 directly regulates the phenotypes observed in *E1A;Hras^{G12V}* MEFs. By overlapping this RNA-seq dataset with a p53 chromatin immunoprecipitation sequencing (ChIP-seq) dataset we previously generated in MEFs (Kenzelmann Broz et al., 2013), we identified 569 p53-dependent genes that are also bound by p53. Of these likely direct targets, 226 are induced or repressed by p53 >1.5-fold (Fig. 7 E and Table S2). Literature analysis of these 226 genes uncovered strong p53-dependent transcriptional signatures relating to p53-dependent phenotypes in *E1A;Hras^{G12V}* MEFs, including apoptosis, genomic fidelity, metabolism, and migration (Fig. 7, F–I). Some categories, such as apoptosis, largely comprised classic p53 target genes (Fig. 7 F), suggesting that these pathways are well characterized. For genome fidelity, we identified genes whose characterized functions relate to processes that p53 is thought only to impact indirectly, such as mitosis (e.g., *Psrc1*, *Mapre3*, and *Dyrk3*; Fig. 7 G; Ban et al., 2009; Jang and Fang, 2011; Rai et al., 2018). For other processes, such as metabolism and migration/invasion, we identified various genes that might contribute to

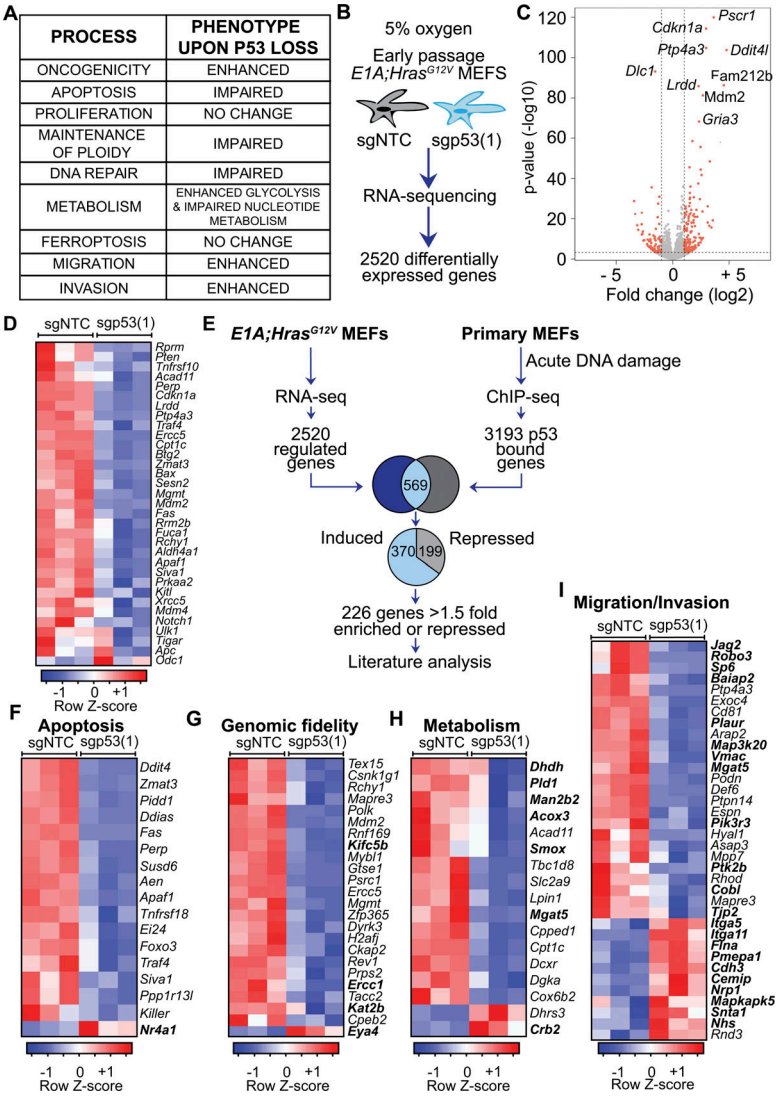

Figure 7. **Gene expression analysis of sgNTC and sgp53(1) *E1A;Hras*^{G12V}*;H11*^{Cas9} MEFs in physiological oxygen. (A)** Loss of p53 induces pleiotropic effects in *E1A;Hras*^{G12V} MEFs in 5% O_2. **(B)** Schematic of RNA-sequencing pipeline of *E1A;Hras*^{G12V} MEFs in 5% O_2. $n = 3$ sgNTC and sgp53(1) targeted cell lines. **(C)** Volcano plot of P value versus fold-change expression of the 2,520 p53-regulated genes identified in RNA-seq analysis. Dots represent genes, and red dots indicate genes with a q value ≤0.05 and a fold-change ≥1.5. **(D)** Heatmap showing expression of well-characterized p53 target genes identified in RNA-seq analysis of sgNTC and sgp53(1)-targeted *E1A;Hras*^{G12V} MEFs (q value ≤0.05; no fold change cutoff). **(E)** Scheme for identifying direct p53 target genes by overlapping *E1A;Hras*^{G12V} RNA-seq data and p53 ChIP-sequencing data from primary MEFs treated with acute DNA damage (Kenzelmann Broz et al., 2013). **(F–I)** Heat maps showing gene expression signatures in sgNTC and sgp53(1)-targeted *E1A;Hras*^{G12V} MEFs for apoptosis (F), genomic fidelity/DNA repair (G), metabolic regulation (H), and migration and invasion (I) identified through literature analysis of the 226 genes that were p53-bound and >1.5-fold induced or repressed in *E1A;Hras*^{G12V} MEFs. Bolded genes were not previously identified as direct p53 targets in mouse or human in a meta-analyses of p53 expression profiling datasets (Fischer, 2019).

the phenotypes we observed but not previously annotated as direct p53 targets (Fig. 7, H and I; Fischer, 2019). The *E1A;Hras*^{G12V} MEF platform can therefore serve as a tool to identify novel p53-regulated genes in diverse p53-dependent processes.

p53 regulates actin dynamics through RhoD

We next sought to determine whether our platform could reveal underappreciated aspects of p53 biology using functional annotation of the 569 p53-bound and regulated genes. Using Enrichr, we identified canonical p53 signatures, as well as noncanonical signatures, such as chromatin/nucleosome remodeling and endosome formation (Fig. 8 A; Chen et al., 2013; Kuleshov et al., 2016). Of relevance to our findings demonstrating a role for p53 in inhibiting cell migration and invasion, we observed numerous signatures relating to actin dynamics, stress fibers, and the cytoskeleton, and identified a list of 57 p53-bound and regulated genes implicated in actin-related processes (Fig. 8, A and B). To determine whether these signatures reflected a clear functional outcome in these cells, we examined F-actin in sgNTC- and sgp53-targeted *E1A;Hras*^{G12V} MEFs. We observed gross alterations in F-actin structure, with a significantly increased percentage of cells with more than five stress fibers per cell in sgp53-targeted cells (40–50%) than in sgNTC cells (<5%; Fig. 8, C and D). Notably, no significant difference was observed in the overall level of F-actin fluorescence between sgNTC- and sgp53-targeted cells, suggesting that differences in stress fiber number cannot be explained by altered levels of F-actin (Fig. 8 E). Instead, functional p53 is associated with reduced stress fibers.

To identify p53 target genes that might be involved in regulating this stress fiber phenotype, we inspected the list of actin-related genes (Fig. 8 B). On this list, we identified three members of the Rho GTPase family known to modulate stress fiber formation: RhoD, RhoV (up-regulated), and RhoE (down-regulated). To hone in on the most relevant family member, we performed meta-analysis of five mouse and five human published RNA-seq and ChIP-seq datasets and observed that RhoD was the Rho GTPase most consistently bound and regulated by p53 across cell types and species (Fig. S4). Inspection of mouse and human p53 ChIP-seq datasets from doxorubicin-treated MEFs and human keratinocytes (Kenzelmann Broz et al., 2013; McDade et al., 2014) revealed p53-binding peaks containing p53

A Enrichr analysis: 569 p53 bound and regulated genes

Index	KEGG 2019 Human	Overlap	Adj. p value
1	p53 signaling pathway	17/72	3.39E-9
Index	**KEGG 2019 MOUSE**	**Overlap**	**Adj. p value**
1	p53 signaling pathway	16/71	2.89E-8
Index	**GO_Cell Component**	**Overlap**	**Adj. p value**
1	**focal adhesion**	31/357	1.07E-8
2	SWI/SNF complex	5/16	8.23E-3
3	BAF-type complex	5/18	1.02E-2
4	npBAF complex	4/12	1.78E-2
5	**actomyosin**	7/49	2.36E-2
6	**contractile actin filament bundle**	6/41	3.47E-2
7	**stress fiber**	6/41	3.47E-2
8	**cytoskeleton**	28/521	3.47E-2
9	early endosome	14/223	1.25E-1
10	chromatin	17/297	1.25E-1
11	**actin cytoskeleton**	17/295	1.25E-1

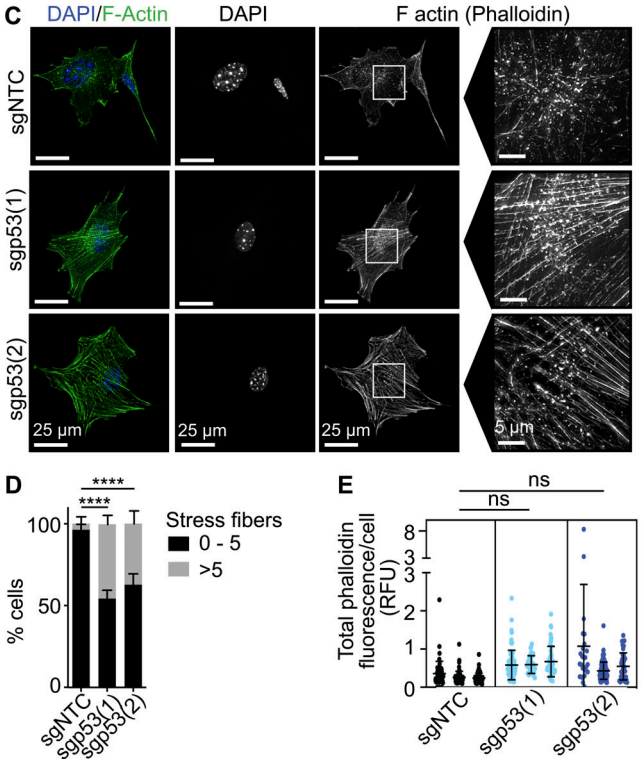

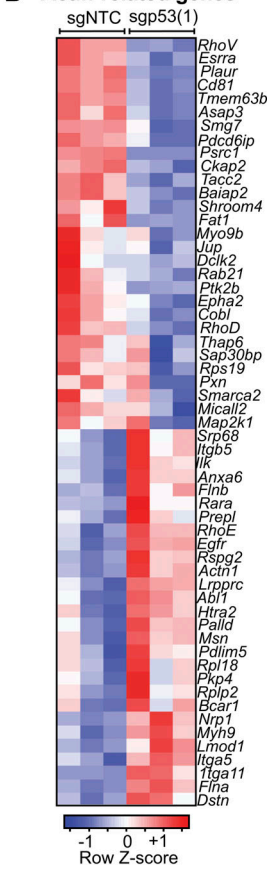

Figure 8. **Loss of p53 enhances stress fiber formation in *E1A;Hras^{G12V};H11^{Cas9}* MEFs.** **(A)** Enrichr analysis of 569 p53-bound and regulated genes identified in RNA-seq analysis of *E1A;Hras^{G12V}* MEFs in 5% O_2. Overlap (hits/total genes in category) and adjusted P values are shown. **(B)** Heatmap showing expression of p53-dependent actin-related genes identified through Enrichr analysis of the *E1A;Hras^{G12V}* MEFs RNA-seq dataset. **(C)** Representative images of F-actin structures stained with phalloidin in *E1A;Hras^{G12V}* MEFs. DAPI marks nuclei. Scale bars, 25 µm and 5 µm (inset). **(D)** Quantitation of sgNTC- and sgp53-targeted *E1A;Hras^{G12V}* MEFs with 0–5 or >5 stress fibers/cell. Data represent the mean ± SD of n = 3 cell lines/sgRNA. ****, P < 0.0001, two-way ANOVA, Tukey's multiple comparison test. **(E)** Total F-actin quantitation by phalloidin staining in sgRNA-targeted *E1A;Hras^{G12V}* MEFs. RFU, relative fluorescence units. Dots represent the total phalloidin fluorescence from one cell, with 35–110 cells analyzed per cell line. n = 3 cell lines/sgRNA. ns, not significant (P > 0.05), nested one-way ANOVA, Tukey's multiple comparisons test. For A–E, all experiments were performed in 5% O_2.

consensus sites within 10 kb of both the mouse and human *RhoD* loci (mouse, in the promoter; human, within intron 1; Fig. 9, A and B). Moreover, we validated p53-dependent expression of *RhoD* in *E1A;Hras^{G12V}* MEFs by qRT-PCR analysis (Fig. 9 C). Together, these results suggest that *RhoD* is a bona fide p53 target gene in both human and mouse cells. To determine whether p53-mediated expression of RhoD can indeed inhibit stress fiber formation, we overexpressed RhoD in p53-deficient *E1A;Hras^{G12V}* MEFs. Overexpression of FLAG-hRHOD significantly decreased the number of stress fibers relative to cells overexpressing HA-GFP (Fig. 9, D and E). These studies thus highlight the regulation of actin dynamics, specifically inhibition of stress fiber formation mediated by RhoD, as an underappreciated aspect of p53 function in cells undergoing cellular transformation.

Collectively, our results suggest that p53 governs a complex network of cellular processes in *E1A;Hras^{G12V}* MEFs, with p53 loss impacting apoptosis, DNA repair, genomic stability, multiple aspects of metabolism, migration, invasion, and actin dynamics (Fig. 9 F). The ability of p53 to coordinately regulate these processes may therefore be integral to its capacity to suppress oncogenic transformation.

Discussion

Here, to gain insight into global p53 function, we examined the ability of p53 to govern a host of cellular processes during transformation suppression. Previous studies characterizing p53 cellular functions have typically described one particular cellular function for p53 in a given context, without a comprehensive analysis to determine whether p53 can act broadly to modulate numerous cellular behaviors in that particular setting. Thus, it remained unclear whether each cellular function that p53 regulates is relevant in a specific context or whether p53 might regulate a range of cellular processes in a particular tumor suppression setting. To test the latter model, we used oncogene-expressing MEFs, expressing or lacking p53, as an in vitro platform to perform a systematic analysis of the impact of p53 loss. Importantly, by using this primary cell-based system, we

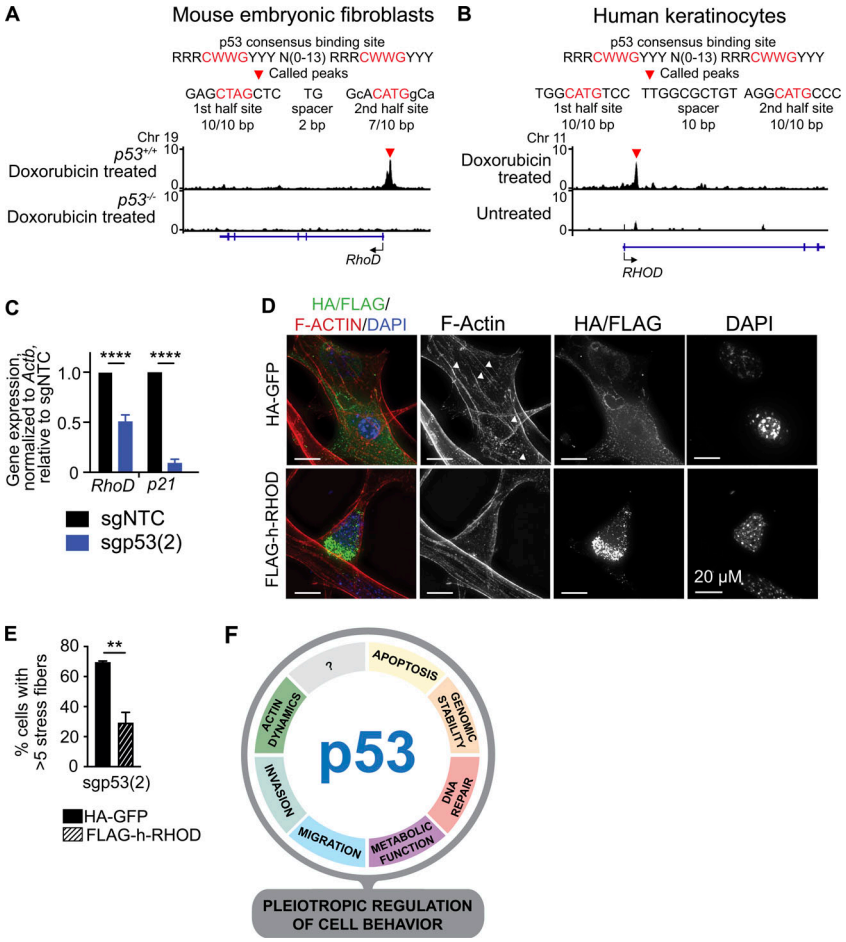

Figure 9. **The p53 target gene RhoD inhibits stress fiber formation in *E1A;Hras^{G12V};H11^{Cas9}* MEFs. (A and B)** p53 ChIP-seq profiles showing peaks in the *RhoD* locus in doxorubicin-treated primary MEFs (Kenzelmann Broz et al., 2013; A) and doxorubicin-treated *TP53$^{+/+}$* human keratinocytes (McDade et al., 2014; B). Exons are indicated by blue boxes, and introns with blue lines. Transcription start sites are marked by arrows. Red triangles mark significant "called" peaks. Predicted p53 response elements in each peak are indicated, with red denoting nucleotides in the conserved C(A/T)(A/T)G core. Spacers between two half sites and number of mismatches (denoted in lower case) are indicated. R = purines A or G; W = A or T; Y = pyrimidines C or T. **(C)** qRT-PCR analysis of *RhoD* and *p21* gene expression in sgNTC and sgp53(2)-targeted *E1A;Hras^{G12V}* MEFs. $n = 2$ cell lines/sgRNA. Data are presented as mean ± SD; ****, $P < 0.0001$, two-way ANOVA, Sidak's multiple comparison test. **(D)** Representative images of phalloidin-stained stress fibers in p53-deficient *E1A;Hras^{G12V}* MEFs overexpressing HA-tagged GFP or FLAG-h-RHOD in 5% O_2. DAPI marks nuclei. Scale bar, 20 µm. **(E)** Percentage of cells with more than five stress fibers in sgp53(2)-targeted *E1A;Hras^{G12V}* MEFs overexpressing HA-GFP or FLAG-h-RHOD in 5% O_2. Data represent mean ± SD of $n = 3$ cell lines. **, $P < 0.01$, unpaired *t* test with Welch's correction. **(F)** The transcription factor p53 modulates a variety of diverse cellular processes in oncogene-expressing MEFs, which may be critical for its capacity to suppress transformation in these cells.

mitigated any effects of accrued mutations typical of cancer cell lines that might confound analyses, and we helped to ensure that p53 signaling pathways remain intact. Consistent with previous studies, we found that p53 loss enhanced anchorage-independent cell growth and protected cells from apoptosis induced by different stressors, validating this model as a tractable system to investigate p53 functions associated with transformation suppression. Beyond these established phenotypes, we now reveal dramatic pleiotropy with p53 deficiency, with widespread alterations in cellular behavior, supporting the idea that in tumor suppression, p53 acts through coordinate regulation of many processes.

An important facet of our study was the analysis of phenotypes at physiological oxygen. With the exception of p53-driven senescence, which is rescued in physiological oxygen (Parrinello et al., 2003), p53 cellular responses in vitro in physiological oxygen have not been well described. Remarkably, some dramatic phenotypes were revealed specifically in low oxygen conditions, including migration and invasion phenotypes observed with p53 deficiency. Thus, by cataloging phenotypes in 5% O_2, which more closely models in vivo conditions, we observe that the contribution of p53 to tumor suppression may be more complex than previously thought.

Among the cellular phenotypes we examined were those described in recent studies implicating specific noncanonical p53 functions in tumor suppression. For example, ferroptosis was proposed as a central mechanism in p53-mediated tumor suppression (Jiang et al., 2015b; Li et al., 2012b). This notion is, however, controversial, with studies showing that p53 is capable of both potentiating and suppressing ferroptosis (Stockwell et al., 2017). Interestingly, in our model, p53 expression did not affect the induction of ferroptosis at 21% O_2. Our observations therefore reinforce the idea that the role of p53 in ferroptosis is cell type specific and suggest further that ferroptosis does not universally explain p53 tumor suppression. Similarly, the capacity to promote DNA repair was proposed to be a critical mechanism by which p53 suppresses tumorigenesis (Janic et al., 2018; Valente et al., 2013). Supporting the idea that p53 promotes DNA repair, we observed delayed DNA double-strand break repair in response to γ-IR in p53-deficient cells. While not necessarily affecting cellular proliferation or survival per se, defective DNA repair upon p53 loss could fuel malignancy by facilitating the accrual of additional mutations during tumor progression.

Beyond contributing to DNA double-strand break repair in our system, p53 exhibits an important role in maintaining chromosomal stability, as we observed significant increases in the numbers of tetraploid, polyploid, and aneuploid cells upon p53 inactivation. The capacity of p53 to regulate mitotic fidelity is thought to largely rely on p21-mediated cell cycle arrest (Kuffer et al., 2013; Lanni and Jacks, 1998). However, we observed no clear effect of p53 loss on proliferation in our system,

presumably because expression of E1A blocks Rb-mediated arrest, the pathway through which p21 acts (Narita et al., 2003). Our findings therefore suggest that the regulation of polyploidy in *E1A;Hras*^{G12V} MEFs occurs through Rb- and cell cycle arrest–independent mechanisms. Intriguingly, our RNA-seq analysis identified several highly up-regulated genes whose encoded proteins have reported roles in mitosis, suggesting that p53 may influence mitotic events directly in these cells. Alternatively, p53 might regulate ploidy though elimination of polyploid cells by apoptosis. Indeed, the Hippo pathway component LATS2 promotes cell death in polyploid E1A- and Hras^{G12V}-expressing human fibroblasts by enhancing p53 activity (Aylon et al., 2010; Ganem et al., 2014). Together, these results highlight an important cell cycle arrest–independent contribution of p53 to the maintenance of genomic fidelity during transformation suppression, another means of impeding malignant progression.

Our study has revealed p53-regulated metabolic processes that may contribute to limiting malignancy under physiological conditions. Previous reports in 21% O_2 have shown that p53 regulates glucose metabolism primarily by inhibiting the Warburg effect, a reprogramming from oxidative respiration to glycolysis characteristic of cancer cells (Vousden and Ryan, 2009). Similarly, we observed that sgp53-targeted *E1A;Hras*^{G12V} MEFs in 5% O_2 exhibited enhanced lactate accumulation and a decreased propensity to convert pyruvate to citrate relative to sgNTC cells. Notably, we observed marked differences in glucose metabolism between 5% and 21% O_2 tensions, with lactate production from glucose being highly favored under physiological oxygen conditions and citrate production favored in atmospheric oxygen. Moreover, the capacity of p53 to inhibit metabolic changes associated with the Warburg effect was greatly dampened in 21% O_2. Thus, previous studies in 21% O_2 may have underestimated p53's contribution to inhibition of the Warburg effect, again highlighting the value of using physiological oxygen tensions during cell culture to accurately model in vivo cell behavior.

In addition to glucose metabolism, p53 regulates other metabolic pathways such as fatty acid oxidation and serine and one-carbon metabolism (Jiang et al., 2015a; Vousden and Ryan, 2009). Metabolomics analysis on *E1A;Hras*^{G12V} MEFs in 5% O_2 revealed that pyrimidine and purine metabolism were severely impacted by p53 loss, supporting several studies documenting altered nucleotide levels upon p53 loss (Huang et al., 2018b; Maddocks et al., 2013). The decreased pyrimidine and purine levels we observe with p53 loss may reflect impaired nucleotide synthesis, defective salvage and uptake pathways, or enhanced utilization of nucleotides—an observation consistent with the need to synthesize an entire genome's worth of extra DNA in tetraploid cells. Together, our results underscore the complexity of p53's regulation of metabolism, with p53 rewiring multiple aspects of glucose and nucleotide metabolism in *E1A;Hras*^{G12V} MEFs.

Although dysregulation of the aforementioned cell processes might contribute to the growth of tumors, we also identified functions regulated by p53 that could be more relevant for metastatic spread. Mutation of *TP53* in human cancers has been correlated with enhanced aggressiveness and metastatic capacity, but the role of p53 in modulating cell migration and invasion has more consistently been linked to p53 gain-of-function rather loss-of-function (Muller et al., 2011). However, some reports suggest a role for WT p53 in dampening both cell migration and invasion, through multiple mechanisms, including inhibition of podosome and filopodia formation and regulation of cell spreading (Kawauchi and Wolf, 2014; Muller et al., 2011). Of note, in our RNA-seq and ChIP-seq analyses, where actin-related functions were among the top molecular signatures, the previously described p53 target genes *Rad* and *Rap2B* (Di et al., 2015; Hsiao et al., 2011) encoding actin regulators were either absent or only mildly enriched. Instead, we identified the RhoGTPase, RhoD, as a key component of p53-dependent regulation of the actin cytoskeleton, with p53-dependent induction conserved between mouse and human cells and RhoD overexpression potently suppressing stress fiber formation in p53-deficient *E1A;Hras*^{G12V} MEFs. Regulation of different types of actin filament assemblies is critical for multiple cell processes, such as mitosis and cytokinesis, establishing polarity, and intracellular trafficking (Pollard and Cooper, 2009; Tojkander et al., 2012). Altered expression of actin-binding proteins, including those regulating stress fiber formation, has been associated with enhanced proliferation, invasion, and metastasis (Liang et al., 2011; Stevenson et al., 2012; Tavares et al., 2017). Transcriptional regulation of *RhoD* and genes encoding other actin-binding proteins by p53, as identified in our RNA-seq analyses, could thus form a critical node in tumor suppression, with the complex interplay between these processes promoting an antitumor program.

It will be important in the future to determine how broadly p53 deficiency drives global phenotypic changes in different cellular contexts. As a proof-of-concept, we show that HCT116 human colon carcinoma cells exhibit dysregulation of multiple cellular processes upon p53 loss, including apoptosis, maintenance of ploidy and glucose metabolism. However, the spectrum of cell processes impacted by p53 deficiency was substantially dampened in HCT116 cells, suggesting selection against p53 signaling during long-term culture. These observations therefore reinforce the value of using a primary cell-based transformation model system, such as *E1A;Hras*^{G12V} MEFs, where the immediate effects of p53 deficiency can be directly assessed. Our HCT116 studies nonetheless support the notion that pleiotropy in p53 function is conserved between species and differentiation states.

Collectively, our findings provide clear evidence that, beyond merely regulating cellular expansion, in this case through apoptosis, p53 can simultaneously regulate numerous other processes, including genome stabilization, DNA repair, metabolism, migration, invasion, and actin dynamics. These observations suggest that during tumor suppression, p53 may govern myriad processes to maintain tissue homeostasis. It will be important to determine whether cooperative regulation of all or only some of these cellular processes is essential for p53 to block tumorigenesis. Such concerted effects may explain why p53, rather than its target genes, is the most frequently mutated gene in human cancer: a single missense mutation in *p53* can trigger an array of pro-tumorigenic changes in nascent cancer cells. It is

interesting to consider the interplay between defects in different processes that could amplify the negative outcomes of p53 loss. For example, loss of p53 increases ploidy and decreases nucleotide availability, which could affect DNA replication by inducing replication fork stalling, leading to increased DNA damage (Bester et al., 2011). These effects would then be further amplified due to impaired DNA repair in cells lacking p53, leading to enhanced mutational rates and promoting more aggressive disease. In addition, although our study uncovers the potential of p53 to regulate many diverse aspects of cellular behavior, the relevance of loss of these functions with *p53* mutation in cancer may depend on tumor stage or microenvironmental cues. Understanding the complex spectrum of cellular activities regulated by p53 in each cell type during transformation suppression will provide insight into the cellular pathways that are best targeted in drug development for different cancer types, either alone or in a synthetic lethal approach.

Materials and methods

Mice

All animal experiments were performed in accordance with the Stanford University Administrative Panel on Laboratory Animal Care. *H11*$^{LSL\text{-}Cas9}$ mice in which expression of Cas9 from the H11 promoter is under control of a *Lox-Stop-Lox* (LSL) cassette were obtained from Monte Winslow (Stanford University, Stanford, CA; Chiou et al., 2015) and crossed with *CMV-Cre* mice (in which expression of Cre-recombinase is under control of the ubiquitous CMV promoter; Schwenk et al., 1995) to recombine the LSL element and generate progeny constitutively expressing Cas9 under control of the *H11* promoter (*H11*^{Cas9}*;CMV-Cre*). *H11*$^{Cas9/+}$*; CMV-Cre/+* mice were then crossed with WT females to generate *H11*^{Cas9} mice, and embryos were harvested at embryonic day 13.5 (E13.5) to prepare MEFs as described. Briefly, embryo body wall tissue was minced using a scalpel. Tissue was dissociated in trypsin for 30 min at 37°C, then dispersed by pipetting, before cells were plated into complete DMEM and allowed to grow in 37°C, 5% CO_2, and 5% O_2 (Johnson et al., 2005). Genotyping to confirm the presence of the *H11-Cas9* transgene and absence of the *CMV-Cre* transgene was performed using the following forward and reverse primers: *Cas9-H11*, 5′-CGGCCGCCACTCGAC GATGTA-3′; *H11* forward, 5′-GGGGCCTCCAAGTCTTGACAGTAG AT-3′; *H11* reverse, 5′-CTGACCAGTGGGACTGCTTTTTCCAG-3′; *Cas9* internal forward, 5′-AGTCTATCCTGCCCAAGAGGAACA GC-3′, *Cas9* internal reverse, 5′-ATAGTGGCTGGCCAGGTACAG GAAGT-3′; *Cre* forward, 5′-TGGGCGGCATGGTGCAAGTT-3′; and *Cre* reverse, 5′-CGGTTGCTAACCAGCGTTTTC-3′.

Generation of isogenic, polyclonal p53 WT, and *p53*-null *E1A; Hras*^{G12V} MEFs

Cells were cultured in high glucose (4.5 g/liter), sodium pyruvate (1 mM), DMEM (Gibco) containing 10% FBS (Sigma-Aldrich), and 100 µg/ml penicillin/streptomycin (Gibco), referred to herein as "complete medium" for all experiments unless otherwise stated. During cell line generation and subsequent experiments (except where noted) cells were maintained at 5% O_2, 5% CO_2, and 37°C. Primary MEFs that were generated from E13.5 *H11*^{Cas9} mice were transduced with E1A- and Hras^{G12V}-expressing retroviruses (pWZL hygro-12S-E1A and pBabe neo-HrasG12V, respectively). Briefly, DNA solutions containing 2 µg of VSV-Env and GAG-POL (retroviral packaging vectors) and 4 µg of plasmid vector in 500 µl of 250 mM $CaCl_2$ were prepared. DNA was then precipitated via addition to 2× Hepes-buffered saline (HBS; 274 mM NaCl, 10 mM KCl, 1.4 mM Na_2HPO_4, 15 mM D-glucose, and 42 mM Hepes, pH 7.05) in a dropwise fashion while aerating the solution. Precipitated DNA was added dropwise to plates of 293AH cells in complete DMEM supplemented with 100 mM chloroquine. Cells were incubated at 37°C, 5% CO_2, and 5% O_2. After 48 h, viral supernatant from these cells was collected and filtered through a 0.4-µm filter. Viral supernatants were mixed at a 1:1 ratio and used to infect primary MEFs (three infections over 48 h). Hygromycin and neomycin selection (~72 h) was used to isolate positively transduced cells. To generate sgRNA-targeted *E1A;Hras*^{G12V} cell lines, passage 2 *E1A;Hras*^{G12V} cell lines were transfected with viral supernatants prepared from 293AH cells transduced with 2 µg VSV-G and delta8.2 (lentiviral packaging vectors) and 4 µg of the lentiviral sgRNA constructs (Transomics, pCLIP-gRNA-EFS-Blast V74) expressing sgRNAs directed against *p53* (sgp53(1), TEVM-11152982, and sgp53(2), TEVM-1220124; see Fig. S1 A for sgRNA sequences) or nontargeting control (sgNTC, pClip-All-EFS-Blast, CAMS1001-22059), as described above. Cells were grown for 7 d to allow for Cas9-mediated cutting of the *p53* locus. Use of multiple guides directed toward *p53* allows for identification and exclusion of phenotypes arising from off-target effects.

To confirm CRISPR/Cas9 targeting of *p53*, forward and reverse primers were designed to amplify the region flanking both sgRNAs' targeting sites in Exon 4 (*p53* forward 5′-GGACTGCAG GGTCTCAGAAG-3′; and *p53* reverse 5′-CTGAAGAGGACCCCC CAAAT-3′), and Sanger sequencing was performed. Sequencing reads were analyzed using interference of CRISPR edits (ICE) algorithm (Synthego) to determine the success of targeting. All sgp53-targeted cell lines exhibited knockout scores of >80 (Fig. S1 B). One sgp53(1) targeted cell line (line 2, embryo 1,588.5) exhibited expression of a protein migrating with p53 (Fig. S1 C) but was unable to induce expression of p21 and Mdm2 (Fig. S1 D), indicating it was functionally null for *p53*. Moreover, the cell line did not significantly differ from the two other completely null sgp53(1) cell lines in any assay performed (Fig. S1, A–F). To confirm on a broader level that this cell line was functionally *p53* null, we chose this sgp53(1) guide for our RNA-seq analyses and observed no or minimal differences from the two completely null sgp53(1) cell lines when assessing p53-target gene expression (Fig. 7 D), again confirming the functionally null status of this line.

If prioritization of a single sgRNA was required, e.g., metabolomics, glucose-tracing, and actin and oxygen tension analyses, we chose to use the sgp53(2) guide given that three of three cell lines were completely *p53* null, thus providing the cleanest system to assess the impacts of p53 loss (Fig. S1 C). Early passages of targeted cells (passages 2–3) were grown in bulk and frozen for future experiments. All phenotypic analyses were performed within 3 wk of thawing cells

(<passage 15) to limit acquisition of phenotypes that were secondary to p53 deficiency.

Physiological versus atmospheric oxygen tension analyses

Frozen vials of sgNTC and sgp53(2) *E1A;Hras*^{G12V} MEFs (generated under 5% O_2 conditions) were thawed and pelleted. Cells were resuspended in medium, and each vial was split in two separate plates. Cells were then incubated in 5% or 21% O_2 incubators (5% CO_2, 37°C) and allowed to equilibrate for a minimum of 72 h (at least one passage) before phenotypic analyses.

Immunoblotting

Protein was extracted from cells using NP-40 lysis buffer (50 mM Tris, pH 8.0, 150 mM NaCl, 1% NP-40, 0.5 mM EDTA, and 10% glycerol) containing Roche cOmplete protease inhibitors. Protein was quantitated using the bicinchoninic acid assay kit (Pierce). 20 µg of protein was resolved on a 10% SDS-PAGE gel, blotted onto polyvinylidene difluoride membranes (Millipore), and blocked in 5% nonfat dry milk prepared in TBS with 0.1% Tween 20 (TBST). Washes were performed in TBST, and the following primary and secondary antibodies were used: rabbit anti-p53 (CM5; Novogene, 1:2,000), rabbit anti-p21 (ab188224; Abcam, 1:1,000), mouse anti-Mdm2 (ab16895; Abcam, 1:500), mouse anti-Gapdh (10R-G109A; Fitzgerald, 1:10,000), peroxidase Affinipure goat anti-rabbit (111-035-144; Jackson Immuno Research, 1:5,000), or goat anti-mouse IgG HRP-conjugated (115-035-003; Jackson Immuno Research, 1:5,000). Immunodetection was performed using ECL Western Blotting substrate (Pierce).

Immunofluorescence

Cells were grown on coverslips for 24 h before the beginning of the experiment. Coverslips were harvested and fixed with 4% PFA, permeabilized with 0.02% Triton X-100 in PBS, and blocked in 5% BSA with the primary and secondary antibodies listed in the relevant methods sections. Coverslips were then mounted using ProLongGold antifade reagent with DAPI (P36931; Invitrogen), unless stated otherwise. For detection of p53 protein expression, primary rabbit anti-p53 (CM5; Novogene, 1:2,000) and secondary Alexa Fluor 546 goat anti-rabbit IgG (A-11035; Invitrogen, 1:250) antibodies were used.

qRT-PCR

RNA was extracted from cells using Trizol reagent (Thermo Fisher Scientific), and cDNA synthesis was performed using Moloney murine leukemia virus reverse transcription (Thermo Fisher Scientific). qRT-PCR (in triplicate) was performed using Power SYBR Green master mix (Thermo Fisher Scientific) using a 7900HT Fast Real-Time PCR machine (Applied Biosystems). The following forward and reverse primers were used: *Cdkn1a/p21* (5′-CACAGCTCAGTGGACTGGAA-3′, 5′-ACCCTAGACCCACAATGCAG-3′), *Bbc3/Puma* (5′-GCGGCGGAGACAAGAAGA-3′, 5′-AGTCCCATGAAGAGATTGTACATGAC-3′), *RhoD* (5′-ATTGTTGTGGGCTGCAAGATA-3′, 5′-CGAGCTGAACACTCAAGATAGG-3′) and *Actb* (5′-TCCTAGCACCATGAAGATCAAGATC-3′, 5′-CTGCTTGCTGATCCACATCTG-3′). Transcript abundance was calculated using a standard curve and normalized to *Actb*.

Soft agar assay

Anchorage-independent growth was assessed using soft agar assays. Briefly, 1.5 ml of phenol-free complete DMEM supplemented with 0.5% low melt agarose (BP160; Fisher) and 10 µg/ml gentamicin was aliquoted into six-well plates (in triplicate) and allowed to set at RT. Next, trypsinized, washed, and pelleted cells were resuspended in phenol-free complete DMEM supplemented with 0.3% noble agar and 10 µg/ml gentamicin at a final density of ∼5,000 cells/1.5 ml. 1.5 ml of cells were then overlaid, in triplicate, onto prepared wells and allowed to set at RT before being overlaid with 1 ml complete DMEM. Cells were incubated at 37°C and 5% CO_2 and either 5% or 21% O_2 for 2 wk, and medium was refreshed once a week. Colonies were visualized by incubation with Giemsa stain (48900; Sigma-Aldrich) for 15 min at RT, then incubation overnight at 4°C. Plates were scanned using an Epson Perfection 3490/3590 scanner, and images were captured at 600-dpi resolution using EpsonScan software. To quantitate colonies, a 400 × 400-pixel square was isolated from the center of each well, and the number of colonies counted using ImageJ (National Institutes of Health).

Cell viability assays

Cells were treated with doxorubicin (0.2 µg/ml) or low-FBS DMEM (0.1% FBS) for 24 h. For 0.1% FBS experiments, cells were washed 3× with warm PBS to remove any residual FCS before addition of 0.1% FBS medium. Cells were harvested by trypsinization and stained with Annexin-V-FITC (BioLegend, 1:40) and propidium iodide (PI; Promocell, 1 µg/ml). Flow cytometric analysis on a BD LSR Fortessa flow cytometer was used to assess cell viability, with events captured using BD FACSDiva software and sample data analyzed using FlowJo 10.5.3 analysis software (FlowJo). Cell viability is expressed relative to DMSO or 10% FBS medium-treated controls.

Proliferation analysis

50,000 cells were plated in six-well plates in duplicate. At 24, 48, 72, and 96 h, duplicate wells were trypsinized, pelleted, resuspended in 1 ml of PBS, and counted using a LUNA II Automated cell counter. The t = 24 h time point served as a starting cell count to control for any differences in seeding potential between cell lines. Fold change in cell number was calculated by dividing the average cell count at each time point (t = 48, 72, and 96 h) by the t = 24 h cell count.

Metaphase spreads

Cells were treated with 10 µg/ml KaryoMAX Colcemid Solution (Gibco) for 2 h. Trypsinized cells were then incubated in 0.56% KCl at RT for 20 min. Cells were fixed in ice-cold 3:1 methanol: glacial acetic acid solution (5 min) and then pelleted on low speed (500 rpm) three times. Cells were dropped on glass slides from ∼1-m height, dried and stained with 3% Giemsa stain (Promega), and coverslips were mounted. Metaphase spreads were captured using a Leica DM6000B bright-field microscope using a Leica 100×/1.4 oil-immersion objective. Images were captured using a Hamamatsu C11440-42U digital camera and Leica Application Suite X (LASX) software. Chromosome number was quantitated in >20 cells per sgRNA per cell line.

Analysis of ploidy using the FUCCI cell cycle marker system

To generate sgNTC- and sgp53-targeted *E1A;Hras^{G12V}* MEF lines expressing the FUCCI system, 293AH cells were transfected with 2 µg retroviral packaging vectors and 4 µg hCDT1-mKO2 or hGeminin-mAG retroviral constructs (Sakaue-Sawano et al., 2008) in 500 µl Opti-MEM (Gibco) mixed with 20 µl Lipofectamine 2000 reagent (Invitrogen) in 480 µl Opti-MEM. A 1:1 hCDT1/hGEM ratio of viral supernatant was used to transduce sgNTC- and sgp53-targeted *E1A;Hras^{G12V}* cells. Transduced cells were cultured for 1 wk before analysis. 100,000 cells were plated into six-well plates, and after 24 h cells were trypsinized, pelleted, resuspended in 1 ml complete DMEM containing DyeCycleViolet reagent (Genesee, 1:1,000), and incubated at 37°C for 30 min before flow cytometric analysis on a BD LSRFortessa X-20 flow cytometer using BD FACSDiva software to capture events. To quantify G_1 tetraploid and polyploidy, samples were analyzed using FlowJo 10.5.3 software. Live cell populations were gated on forward/side scatter scatterplots; live cells were then plotted on a mKO_2/mAG scatterplot, and cells positive for either marker were gated (FUCCI$^+$ cells). DNA content of FUCCI$^+$ cells was then plotted on a histogram using DyeCycleViolet fluorescence, and gates were drawn around cells exhibiting ≥2N DNA content (>2N cells). Finally, >2N cells were plotted on an mKO_2/mAG scatterplot. G_1 tetraploid cells were defined as cells having >2N DNA expressing hCDT1-mKO_2, and polyploid cells were defined as having >4N DNA content.

Live-cell imaging of mitosis and migration

Cells in complete DMEM minus phenol red were plated in Ibidi µ-slide eight-chamber glass-bottom culture slides precoated with poly-D-lysine (5 µg/cm^2). Cells were imaged by phase contrast at intervals of 5 min for 16 h on a Leica DMi8 inverted microscope set on a 63×/1.4 magnification oil objective using a Leica DFC9000 GT digital camera and LASX software. 10 regions of the culture chamber were imaged and analyzed per cell line, with >45 cells analyzed for all lines. Normal mitotic events were defined by cells balling up and then splitting into two daughter cells, whereas abnormal mitotic events were determined by the following criteria: multipolar mitosis (cell splits or attempts to split into >2 cells); mitotic slippage and failed cytokinesis (cell balls up but then flattens without splitting into daughter cells, or attempts to split but then fails), bi/multinucleation (cells undergo mitosis and daughter cells have more than one nucleus), or bi/multinucleate recovery (cells with more than one nucleus ball up and split into two or more cells with daughter cells having one or more nuclei).

Quantitation of multinucleated cells

Cells were grown on coverslips at low density in complete DMEM for 24 h. Cells were then fixed, permeabilized, and stained with Alexa Fluor 488 wheat germ agglutinin (WGA; W11261; Fisher, 1:1,000) to define cell boundaries, and then mounted on slides using ProLongGold antifade reagent with DAPI (P36931; Invitrogen) to visualize DNA. Cells were imaged on a Leica DMi8 inverted fluorescence microscope using a Leica 63×/1.4 oil objective, with an 8 × 8 tile scan captured using a Leica DFC9000GT digital camera and LASX acquisition software. The number of nuclei per cell was then manually quantified.

BrdU proliferation analysis

Cells were pulsed for 1 h with BrdU (555627; BD Pharminogen, 1:50) before being fixed, permeabilized, treated with 1.5N HCl, blocked in 5% BSA, and stained with antibodies toward BrdU (ab152095; Abcam, 1:50) and Alexa Fluor 546 goat anti-mouse IgG (A-11003; Invitrogen, 1:250). Cells were visualized using a Leica DM600B fluorescent microscope and a 40×/0.85 dry objective. Images were captured using a Hamamatsu C11440-42U digital camera and LASX acquisition software. BrdU$^+$ cells were quantified using ImageJ.

Quantitation of DNA repair by γH2AX foci resolution assay

Cells were irradiated with 2 Gy IR using a ^{137}Cs source. Unirradiated cells served as controls. At 1, 6, and 24 h after IR, cells were subjected to immunofluorescence analysis (see above) using antibodies against phosphorylated histone H2AX-Ser139 (JBW-301; Millipore, 1:1,000) and fluorescein goat anti-mouse IgG (FI-2000; Invitrogen, 1:250). Cells were visualized using a Leica DM6000B fluorescent microscope with a 40×/0.85 dry objective. Images were captured using a Hamamatsu C11440-42U digital camera and LASX software. Five images/time point were captured and analyzed using ImageJ. Quantification of total γH2AX fluorescence per nucleus was performed rather than counting individual γH2AX foci to account for differences in the total number, size, and intensity of γH2AX foci between different cells. To control for potential differences in the total size of nuclei between WT and p53-deficient cells, γH2AX fluorescence values were normalized to the nuclear area by region of interest gating on DAPI fluorescence, and the percentage of cells exhibiting high γH2AX fluorescence was quantitated. To set the threshold cutoff for γH2AX^{high} cells, we quantitated the γH2AX fluorescence of sgNTC-targeted cells 1 h after 2 Gy IR and then performed statistical analysis (descriptive statistics algorithm, Prism 8) to determine the upper 75th percentile quartile. Any γH2AX fluorescence value in the 75th percentile quartile was then determined to be γH2AX^{high}. This threshold (sgNTC 1 h after treatment) was then applied to all cell lines and time points. Data represent three independent cell lines/sgRNA, and >50 cells were analyzed per cell line and time point.

Ferroptosis analysis

Erastin2 (compound 35MEW28, reported in Dixon et al., 2014) was synthesized by Acme Bioscience (Palo Alto, CA), and Ferrostatin-1 was obtained from Cayman Chemicals. Both drugs were resuspended in DMSO and stored at −20°C before use. For ferroptosis analysis using PI at 5% O_2 tension, cells were treated with 10 or 100 nM erastin2 ± 1 µM ferrostatin-1 for 16 h. Cells were harvested by trypsinization and then stained with PI (Promocell, 1 µg/ml). Flow cytometric analysis of cell viability was performed using a BD LSR Fortessa flow cytometer with events captured using BD FACSDiva software. Sample data were analyzed using FlowJo 10.5.3 analysis software (FlowJo). Ferroptosis susceptibility at 21% O_2 tension was assayed using STACK (scalable time-lapse analysis of cell death kinetics;

Forcina et al., 2017). *E1A;Hras*^{G12V} sgNTC- or sgp53-targeted MEFs were transduced with a nuclear localized NucLight Red lentiviral construct (NLR, IncuCyte) encoding a nuclear-localized mKate2 protein, and positively transduced cells were selected using puromycin selection. mKate2$^+$ *E1A;Hras*^{G12V} sgNTC- or sgp53-targeted MEFs were seeded in replicate in 96-well plates at a density of 15,000 (sgNTC) or 10,000 (sgp53(1) and sgp53(2)) cells per well. Lower cell densities for sgp53(1) and sgp53(2) cells were used to ensure equal cell density given that sgp53-targeted cells exhibit a higher total area and seeding efficiency than sgNTC-targeted cells. The next day, each replicate plate was treated with erastin2 or a vehicle control in a 4-point 10-fold series of doses (100 nM down to 0.1 nM). Each replicate plate was then cotreated with either 1 µM ferrostatin-1 or vehicle. SYTOX Green viability dye (Life Technologies) at a final concentration of 22 nM was also added to each well of all plates. Cells were imaged at t = 0, 4, 8, and 24 h using an IncuCyte live cell analyzer (Essen BioScience). mKate2$^+$, SYTOX Green$^+$, and double-positive mKate2$^+$/SYTOX Green$^+$ objects were counted using IncuCyte ZOOM Live-Cell Analysis System software. Lethal fraction scores were calculated for each time point (Forcina et al., 2017) with the following modification: double-positive (mKate2$^+$/SYTOX Green$^+$) cells were subtracted from the counts of live mKate2$^+$ cells at all time points.

Lipid peroxidation flow cytometric analysis

E1A;Hras^{G12V} MEFs were cultured in 5% or 21% O_2 for 72 h before harvesting by trypsinization. Cells were then stained with the BODIPY 581/591 C11 lipid peroxidation sensor (D3861 Thermo Fisher Scientific) for 30 min at 37°C (5% or 21% O_2) before flow cytometric analysis on a BD LSRFortessa X-20 flow cytometer using BD FACSDiva software to capture events. Live cells were plotted on PE-Texas Red versus FITC dot plots, with PE Texas Red$^+$/FITC$^+$ cells serving as the positive population. Unstained cells served as a gating control.

[U-^{13}C]glucose tracing

Cells were equilibrated in RPMI 1640 with 10% dialyzed FBS (Thermo Fisher Scientific) for 48 h before the assay. For oxygen tension experiments, cells were thawed into this medium and allowed to equilibrate in 5% or 21% O_2 for 72 h before plating for analysis. Cells were washed twice with warm sterile PBS before [U-^{13}C]glucose RPMI medium (10% dialyzed FBS) lacking glucose, serine, and glycine (TEKnova) and reconstituted with [U^{13}C]glucose (2 g/liter), serine (0.03 g/liter), and glycine (0.01 g/liter) was added to each plate. At 6 h, medium was removed, and plates were washed twice with ice-cold PBS before extraction with 325 µl of 80:20 acetonitrile:water on ice for 15 min. Cells were scraped off plates, sonicated for 30 s with a Biorupter^{300} sonicator (Diagenode), and spun down at 1.5 × 10^4 rpm for 10 min. 200 µl supernatant was taken out for immediate LC/electrospray ionization MS/MS analysis.

Quantitative LC/electrospray ionization MS/MS analysis of [^{13}C]glucose-labeled cell extracts was performed using an Agilent 1290 UHPLC system equipped with an Agilent 6545 quadrupole time-of-flight mass spectrometer. A hydrophilic interaction chromatography method with a BEH amide column (100 × 2.1 mm internal diameter, 1.7 µm; Waters) was used for compound separation at 35°C with a flow rate of 0.3 ml/min. Mobile phase A consisted of 25 mM ammonium acetate and 25 mM ammonium hydroxide in water, and mobile phase B was acetonitrile. The gradient elution was 0–1 min, 85% B; 1–12 min, 85% B → 65% B; 12–12.2 min, 65% B → 40% B; 12.2–15 min, 40% B. After the gradient, the column was reequilibrated at 85% B for 5 min. The overall runtime was 20 min, and the injection volume was 5 µl. Agilent quadrupole time-of-flight was operated in negative mode, and the relevant parameters were ion spray voltage, 3,500 V; nozzle voltage, 1,000 V; fragmentor voltage, 125 V; drying gas flow, 11 liter/min; capillary temperature, 325°C; drying gas temperature, 350°C; and nebulizer pressure, 40 psi. A full scan range was set at 50 to 1,600 m/z. The reference masses were 119.0363 and 980.0164. The acquisition rate was 2 spectra/s. Isotopologue extraction was performed in an Agilent Profinder B.08.00 (Agilent Technologies). Retention time of each metabolite was determined by authentic standards. The mass tolerance was set to ±15 ppm, and retention time tolerance was ±0.2 min. Natural isotope abundance was corrected using Agilent Profinder software (Agilent Technologies). For normalization of ion counts, cell pellets were vacuum dried, and then protein concentration was determined using the Pierce bicinchoninic acid protein assay kit (Thermo Fisher Scientific), according to manufacturer's instructions.

Metabolomics analysis

3 × 10^6 sgNTC-targeted and 2 × 10^6 sgp53(2)-targeted *E1A;Hras*^{G12V}*;H11*^{Cas9} MEFs were plated in 10-cm plates in complete DMEM. Different seeding densities were used to account for differences in seeding efficiency and cell size between sgNTC and sgp53(2) cells, ensuring that cells were analyzed when growing exponentially. Cells were analyzed when 80% confluent. At 24 h, cells were fixed and lysed by incubation in 80% methanol on dry ice. Methanol-extracted samples were then processed by the Children's Medical Center Research Institute Metabolomics Core Facility at UT Southwestern. Targeted LC/MS/MS using an AB QTRAP 5500 liquid chromatograph/triple quadrupole mass spectrometry system (AB SCIEX) and data analysis were performed as previously described (Kim et al., 2017; Mullen et al., 2014). Relative metabolite abundances were determined by normalizing peak areas to total ion current. Unpaired Student's t tests were used to determine any statistically significant difference in metabolite concentrations. Pathway enrichment analysis on significant hits was performed using Metaboanalyst 3.0 (Chong et al., 2018).

Transwell Boyden chamber migration assay

Boyden chamber assays were performed with complete DMEM (10% FBS) in the lower compartment of the Transwell plate and 25,000 cells in 500 µl of complete DMEM (10% FBS) in the top compartment (Corning 12-well control inserts, 8-µM pores). Cells were incubated for 24 h before nonmigrating cells were removed, and inserts were fixed in 4% PFA (15 min), washed three times with PBS, and stained with 0.1% crystal violet (Sigma-Aldrich) for 30 min. Washed (H_2O) and dried membranes were then covered with coverslips, and cells were

visualized by bright-field microscopy on a Leica DM6000B microscope using a 20×/0.8 dry objective. Images were captured using a Hamamatsu C11440-42U digital camera and LASX acquisition software. Five images in random positions were captured per insert (excluding the regions closest to the insert edge). Cells per 20× objective field were then quantified.

Collagen 3D matrix invasion assay

A single-cell suspension of 5,000 cells in 100 µl DMEM with 20% FBS was mixed with 100 µl rat tail collagen I (Corning) on ice. 50 µl cell/collagen suspension was then plated into the wells of a 96-well plate in triplicate. Collagen was allowed to polymerize for 30 min at RT before plates were incubated at 37°C, 5% CO_2, and 5% O_2 for 1 h. Collagen plugs were overlaid with 100 µl complete DMEM and incubated for 5 d. Excess media was removed, and collagen plugs were fixed in 4% PFA for 1 h before plugs were permeabilized in 0.02% Triton X-100 in PBS for 30 min. Plugs were washed with PBS three times before being stained with WGA and DAPI (BioLegend, 1:1,000) in PBS overnight at 4°C. Collagen plugs were washed three times in PBS before being plated onto glass slides on which paraffin wax was used to create a hydration barrier, and excess PBS was then added to maintain hydration of the collagen plug during imaging. Collagen plugs were overlaid with a coverslip and sealed with nail polish. Quantitation of invading/non-invading colonies was performed by manually scanning the entire collagen plug by eye using a Leica DMi8 inverted fluorescence microscope, set on a 40×/0.85 dry objective. To create representative images, collagen plugs were imaged on a DM6000B microscope using a 40×/0.85 dry objective, with a Z-stack of the entire colony captured. Images were captured using a Leica DFC9000 GT digital camera and processed using LASX software and the 3D-deconvolution and maximum-projection algorithms.

RNA-seq expression analysis

For RNA-seq, 10^6 cells (three sgNTC and three sgp53(1) cell lines) were plated in complete DMEM and incubated for 24 h at 37°C, 5% CO_2, and 5% O_2. The sgp53(1) sgRNA was used for this RNA-seq analysis to determine the functionality of the protein expressed in embryonic line 2, which migrated at the same size as p53 on SDS-PAGE. Analysis focusing on canonical p53 target genes indicated that this line did not significantly differ from the other two completely null sgp53(1) lines, indicating it was functionally null. RNA-seq libraries were prepared using the Illumina TruSeq Kit (v.2), using 1 µg total RNA for each library. RNA-seq libraries were submitted for sequencing on an Illumina Hiseq 4000 at the Stanford Functional Genomics Facility. The sequence data were filtered for sequence and alignment quality according to the Stanford Functional Genomics Facility's pipeline. Filtered FASTQ files were then submitted to Basespace's RNA Express analysis pipeline (v1.0.0). Briefly, the STAR aligner (Dobin et al., 2013) was used to align the reads to the mouse genome (mm10), and DESEQ2 (Love et al., 2014) was used for differential expression analysis. A volcano plot showing highly significant genes (q value ≤0.05, fold-change ≥1.5) was generated. The q value refers to the P value adjusted for false discovery rate. Genes with a q value of ≤0.05 were used for all subsequent analysis. All RNA-seq data are available in the GEO database, accession no. GSE136355. Previously published p53 ChIP-seq results from primary MEFs treated with 0.2 µg/ml doxorubicin were used to define p53-bound genes and were defined as genes that display p53 binding within 10 kb of the gene. (Kenzelmann Broz et al., 2013), available on the GEO database, accession no. GSE46240. To identify novel p53-direct target genes, we cross-referenced our RNA-seq dataset with the TargetGeneReg database, derived from a meta-analysis of human and mouse p53 expression profiling datasets (Fischer, 2019). Heatmaps were generated using Heatmapper (Babicki et al., 2016). To determine the cell processes in which the 226 genes up- or down-regulated by p53 >1.5-fold had been previously been implicated, annotations on GeneCards, the human gene database (Stelzer et al., 2016), were used to bin genes into functional categories. Categorization was then refined by literature analysis on PubMed. Pathway enrichment analysis was performed using Enrichr (Chen et al., 2013; Kuleshov et al., 2016) using the KEGG 2019 Human, KEGG 2019 Mouse, and GO Cell Component databases. Meta-analysis of RhoGTPase expression in human and mouse RNA-seq and ChIP-seq datasets was derived from the following studies: Allen et al., 2014; Kenzelmann Broz et al., 2013; Lee et al., 2010; Li et al., 2012a; McDade et al., 2014; Menendez et al., 2013; Nikulenkov et al., 2012; Tanikawa et al., 2017; Tonelli et al., 2015; Wang et al., 2014.

Actin structure analysis

For actin structure analysis, cells were grown on coverslips for 24 h, fixed, and permeabilized as described above. Cells were stained with Alexa Fluor 488 Phalloidin (a kind gift from Matt Footer, Stanford University, Stanford, CA; 1:1,000) for 1 h at 37°C in a humidified chamber. Cells were visualized using a Leica DMi8 inverted microscope with a 63×/1.4 oil-immersion objective. Z-stack images were captured and processed using a Leica DFC9000GT digital camera, LASX acquisition software, and 3D-deconvolution and maximum-projection algorithms. Total cell Phalloidin fluorescence was quantified using ImageJ. Briefly, using the Alexa Fluor 488 channel, region of interest gates were drawn around individual cells, and total cell fluorescence and cell area were measured. To account for differences in cell size between sgNTC- and sp53-targeted cells, phalloidin fluorescence values were normalized to total cell area. Stress fiber number was analyzed manually. Total cell phalloidin fluorescence and stress fiber analysis represents the combined analysis of >30 cells per cell line.

hRhoD overexpression

HA-tagged GFP (pcDNA3.1-3XHA-GFP plasmid; Brady et al., 2011) and FLAG (DYKDDDDK)-tagged hRhoD ORF clone (pcDNA3.1+C-(K)-DYK, ABIN4924331, Genomics-Online.com) overexpression constructs were transfected into sgp53(2) *E1A;Hras^{G12V};H11^{Cas9}* MEFs using Lipofectamine 2000 (Invitrogen), as described above. After 24 h, cells were harvested, fixed, permeabilized, and stained with Alexa Fluor 647 Phalloidin (A22287; Thermo Fisher Scientific, 1:1,000) to mark F-actin, mouse anti-FLAG (clone M2 F1804; Sigma-Aldrich, 1:50), mouse anti-HA (12CA5;

Sigma-Aldrich, 1:50), fluorescein goat anti-rabbit IgG (FI-1000; Invitrogen, 1:250), and fluorescein anti-mouse IgG (FI-2000; Invitrogen, 1:250). Cells were visualized using a Leica DMi8 inverted microscope with a 63×/1.4 oil-immersion objective. Z-stack images were captured and processed using a Leica DFC9000 GT digital camera, LASX acquisition software, and 3D-deconvolution and maximum-projection algorithms.

Statistical analysis

Unless otherwise stated, all statistical analyses were performed using GraphPad Prism 8.

Online supplemental material

Fig. S1 shows sgp53 CRISPR targeting sites and validation studies on the nine cell lines used in this study. Fig. S2 shows comparative analysis of cell behavior under physiological (5%) or atmospheric (21%) oxygen conditions. Fig. S3 shows phenotypic analysis of the consequences of p53 loss in human HCT116 colon carcinoma cell lines. Fig. S4 shows meta-analysis of RhoGTPase expression in mouse and human RNA-seq and ChIP-seq datasets. Video 1 shows normal and abnormal mitotic events in sgNTC- and sgp53-targeted *E1A;Hras*^{G12V} MEFs in 5% O_2. Video 2 shows 2D migration of sgNTC- and sgp53-targeted *E1A;Hras*^{G12V} MEFs in 5% O_2. Table S1 shows metabolomics analysis of sgNTC- and sgp53(2)-targeted *E1A;Hras*^{G12V} MEFs generated in 5% O_2. Table S2 shows the differentially expressed genes between sgNTC- and sgp53(1)-targeted *E1A;Hras*^{G12V} MEFs grown in 5% O_2.

Acknowledgments

We thank the following people for the provision of reagents and/or advice with the development of new protocols: Monte M. Winslow, Ian Winters, Edward LaGory, Ejung Moon, Jan Skotheim, and Matt Footer. We are grateful to Lauren Zacharias at the Children's Medical Center Research Institute's Metabolomics Facility at UT Southwestern for running our metabolomics analysis. We thank Julien Sage and Alyssa Kaiser for critical reading of the manuscript.

This study was supported by funding to L.D. Attardi from National Institutes of Health grant R35CA197591, and to R.J. DeBerardinis from National Institutes of Health grant R35CA22044901.

The authors declare no competing financial interests.

Author contributions: Conceptualization, L.J. Valente, R.J. DeBerardinis, J. Ye, S.J. Dixon, and L.D. Attardi; Funding Acquisition, L.D. Attardi; Investigation, L.J. Valente, A. Tarangelo, A.M. Li, M. Naciri, N. Raj, A.M. Boutelle, Y. Li, S.S. Mello, and K. Bieging-Rolett; specifically, A. Tarangelo performed erastin2 treatment experiments and data analysis; A.M. Li and Y. Li ran and analyzed [^{13}C]glucose tracing samples on LC/MS; M. Naciri performed DNA repair, phalloidin expression, and stress fiber quantitation; N. Raj performed p53 target gene Western blotting; A.M. Boutelle aided in proliferation analyses; S.S. Mello performed RNA sequencing analysis, generating the list of differentially expressed genes; and K. Bieging-Rolett generated the *H11*^{Cas9} mice. Writing – Original Draft, L.J. Valente and L.D. Attardi; Supervision, L.D. Attardi.

Submitted: 29 August 2019
Revised: 17 June 2020
Accepted: 28 July 2020

References

Allen, M.A., Z. Andrysik, V.L. Dengler, H.S. Mellert, A. Guarnieri, J.A. Freeman, K.D. Sullivan, M.D. Galbraith, X. Luo, W.L. Kraus, et al. 2014. Global analysis of p53-regulated transcription identifies its direct targets and unexpected regulatory mechanisms. *eLife*. 3. e02200. https://doi.org/10.7554/eLife.02200

Andrysik, Z., M.D. Galbraith, A.L. Guarnieri, S. Zaccara, K.D. Sullivan, A. Pandey, M. MacBeth, A. Inga, and J.M. Espinosa. 2017. Identification of a core TP53 transcriptional program with highly distributed tumor suppressive activity. *Genome Res*. 27:1645–1657. https://doi.org/10.1101/gr.220533.117

Aylon, Y., Y. Ofir-Rosenfeld, N. Yabuta, E. Lapi, H. Nojima, X. Lu, and M. Oren. 2010. The Lats2 tumor suppressor augments p53-mediated apoptosis by promoting the nuclear proapoptotic function of ASPP1. *Genes Dev*. 24:2420–2429. https://doi.org/10.1101/gad.1954410

Babicki, S., D. Arndt, A. Marcu, Y. Liang, J.R. Grant, A. Maciejewski, and D.S. Wishart. 2016. Heatmapper: web-enabled heat mapping for all. *Nucleic Acids Res*. 44(W1):W147–W153. https://doi.org/10.1093/nar/gkw419

Ban, R., H. Matsuzaki, T. Akashi, G. Sakashita, H. Taniguchi, S.Y. Park, H. Tanaka, K. Furukawa, and T. Urano. 2009. Mitotic regulation of the stability of microtubule plus-end tracking protein EB3 by ubiquitin ligase SIAH-1 and Aurora mitotic kinases. *J. Biol. Chem*. 284:28367–28381. https://doi.org/10.1074/jbc.M109.000273

Bester, A.C., M. Roniger, Y.S. Oren, M.M. Im, D. Sarni, M. Chaoat, A. Bensimon, G. Zamir, D.S. Shewach, and B. Kerem. 2011. Nucleotide deficiency promotes genomic instability in early stages of cancer development. *Cell*. 145:435–446. https://doi.org/10.1016/j.cell.2011.03.044

Brady, C.A., D. Jiang, S.S. Mello, T.M. Johnson, L.A. Jarvis, M.M. Kozak, D. Kenzelmann Broz, S. Basak, E.J. Park, M.E. McLaughlin, et al. 2011. Distinct p53 transcriptional programs dictate acute DNA-damage responses and tumor suppression. *Cell*. 145:571–583. https://doi.org/10.1016/j.cell.2011.03.035

Bunz, F., A. Dutriaux, C. Lengauer, T. Waldman, S. Zhou, J.P. Brown, J.M. Sedivy, K.W. Kinzler, and B. Vogelstein. 1998. Requirement for p53 and p21 to sustain G2 arrest after DNA damage. *Science*. 282:1497–1501. https://doi.org/10.1126/science.282.5393.1497

Charni, M., R. Aloni-Grinstein, A. Molchadsky, and V. Rotter. 2017. p53 on the crossroad between regeneration and cancer. *Cell Death Differ*. 24:8–14. https://doi.org/10.1038/cdd.2016.117

Chen, E.Y., C.M. Tan, Y. Kou, Q. Duan, Z. Wang, G.V. Meirelles, N.R. Clark, and A. Ma'ayan. 2013. Enrichr: interactive and collaborative HTML5 gene list enrichment analysis tool. *BMC Bioinformatics*. 14:128. https://doi.org/10.1186/1471-2105-14-128

Chiou, S.H., I.P. Winters, J. Wang, S. Naranjo, C. Dudgeon, F.B. Tamburini, J.J. Brady, D. Yang, B.M. Grüner, C.H. Chuang, et al. 2015. Pancreatic cancer modeling using retrograde viral vector delivery and in vivo CRISPR/Cas9-mediated somatic genome editing. *Genes Dev*. 29:1576–1585. https://doi.org/10.1101/gad.264861.115

Chong, J., O. Soufan, C. Li, I. Caraus, S. Li, G. Bourque, D.S. Wishart, and J. Xia. 2018. MetaboAnalyst 4.0: towards more transparent and integrative metabolomics analysis. *Nucleic Acids Res*. 46(W1):W486–W494. https://doi.org/10.1093/nar/gky310

Christophorou, M.A., I. Ringshausen, A.J. Finch, L.B. Swigart, and G.I. Evan. 2006. The pathological response to DNA damage does not contribute to p53-mediated tumour suppression. *Nature*. 443:214–217. https://doi.org/10.1038/nature05077

Deng, Q., Y. Li, D. Tedesco, R. Liao, G. Fuhrmann, and P. Sun. 2005. The ability of E1A to rescue ras-induced premature senescence and confer transformation relies on inactivation of both p300/CBP and Rb family proteins. *Cancer Res*. 65:8298–8307. https://doi.org/10.1158/0008-5472.CAN-05-0054

Di, J., H. Huang, Y. Wang, D. Qu, J. Tang, Q. Cheng, Z. Lu, Y. Zhang, and J. Zheng. 2015. p53 target gene Rap2B regulates the cytoskeleton and inhibits cell spreading. *J. Cancer Res. Clin. Oncol*. 141:1791–1798. https://doi.org/10.1007/s00432-015-1948-8

Dixon, S.J., K.M. Lemberg, M.R. Lamprecht, R. Skouta, E.M. Zaitsev, C.E. Gleason, D.N. Patel, A.J. Bauer, A.M. Cantley, W.S. Yang, et al. 2012.

Ferroptosis: an iron-dependent form of nonapoptotic cell death. *Cell*. 149:1060–1072. https://doi.org/10.1016/j.cell.2012.03.042

Dixon, S.J., D.N. Patel, M. Welsch, R. Skouta, E.D. Lee, M. Hayano, A.G. Thomas, C.E. Gleason, N.P. Tatonetti, B.S. Slusher, et al. 2014. Pharmacological inhibition of cystine-glutamate exchange induces endoplasmic reticulum stress and ferroptosis. *eLife*. 3. e02523. https://doi.org/10.7554/eLife.02523

Dobin, A., C.A. Davis, F. Schlesinger, J. Drenkow, C. Zaleski, S. Jha, P. Batut, M. Chaisson, and T.R. Gingeras. 2013. STAR: ultrafast universal RNA-seq aligner. *Bioinformatics*. 29:15–21. https://doi.org/10.1093/bioinformatics/bts635

Donehower, L.A., M. Harvey, B.L. Slagle, M.J. McArthur, C.A. Montgomery, Jr., J.S. Butel, and A. Bradley. 1992. Mice deficient for p53 are developmentally normal but susceptible to spontaneous tumours. *Nature*. 356:215–221. https://doi.org/10.1038/356215a0

Efeyan, A., M. Collado, S. Velasco-Miguel, and M. Serrano. 2007. Genetic dissection of the role of p21Cip1/Waf1 in p53-mediated tumour suppression. *Oncogene*. 26:1645–1649. https://doi.org/10.1038/sj.onc.1209972

Eischen, C.M., M.F. Roussel, S.J. Korsmeyer, and J.L. Cleveland. 2001. Bax loss impairs Myc-induced apoptosis and circumvents the selection of p53 mutations during Myc-mediated lymphomagenesis. *Mol. Cell. Biol*. 21:7653–7662. https://doi.org/10.1128/MCB.21.22.7653-7662.2001

Fischer, M.. 2019. Conservation and divergence of the p53 gene regulatory network between mice and humans. *Oncogene*. 38:4095–4109. https://doi.org/10.1038/s41388-019-0706-9

Forcina, G.C., M. Conlon, A. Wells, J.Y. Cao, and S.J. Dixon. 2017. Systematic Quantification of Population Cell Death Kinetics in Mammalian Cells. *Cell Syst*. 4:600–610.e6. https://doi.org/10.1016/j.cels.2017.05.002

Fujiwara, T., M. Bandi, M. Nitta, E.V. Ivanova, R.T. Bronson, and D. Pellman. 2005. Cytokinesis failure generating tetraploids promotes tumorigenesis in p53-null cells. *Nature*. 437:1043–1047. https://doi.org/10.1038/nature04217

Gadea, G., M. de Toledo, C. Anguille, and P. Roux. 2007. Loss of p53 promotes RhoA-ROCK-dependent cell migration and invasion in 3D matrices. *J. Cell Biol*. 178:23–30. https://doi.org/10.1083/jcb.200701120

Ganem, N.J., H. Cornils, S.Y. Chiu, K.P. O'Rourke, J. Arnaud, D. Yimlamai, M. Théry, F.D. Camargo, and D. Pellman. 2014. Cytokinesis failure triggers hippo tumor suppressor pathway activation. *Cell*. 158:833–848. https://doi.org/10.1016/j.cell.2014.06.029

Garrison, S.P., J.R. Jeffers, C. Yang, J.A. Nilsson, M.A. Hall, J.E. Rehg, W. Yue, J. Yu, L. Zhang, M. Onciu, et al. 2008. Selection against PUMA gene expression in Myc-driven B-cell lymphomagenesis. *Mol. Cell. Biol*. 28:5391–5402. https://doi.org/10.1128/MCB.00907-07

Hemann, M.T., J.T. Zilfou, Z. Zhao, D.J. Burgess, G.J. Hannon, and S.W. Lowe. 2004. Suppression of tumorigenesis by the p53 target PUMA. *Proc. Natl. Acad. Sci. USA*. 101:9333–9338. https://doi.org/10.1073/pnas.0403286101

Hinkal, G., N. Parikh, and L.A. Donehower. 2009. Timed somatic deletion of p53 in mice reveals age-associated differences in tumor progression. *PLoS One*. 4. e6654. https://doi.org/10.1371/journal.pone.0006654

Hollstein, M., D. Sidransky, B. Vogelstein, and C.C. Harris. 1991. p53 mutations in human cancers. *Science*. 253:49–53. https://doi.org/10.1126/science.1905840

Hsiao, B.Y., C.C. Chen, P.C. Hsieh, T.K. Chang, Y.C. Yeh, Y.C. Wu, H.S. Hsu, F.F. Wang, and T.Y. Chou. 2011. Rad is a p53 direct transcriptional target that inhibits cell migration and is frequently silenced in lung carcinoma cells. *J. Mol. Med. (Berl.)*. 89:481–492. https://doi.org/10.1007/s00109-010-0717-z

Huang, C., M. Yang, J. Deng, P. Li, W. Su, and R. Jiang. 2018a. Upregulation and activation of p53 by erastin-induced reactive oxygen species contribute to cytotoxic and cytostatic effects in A549 lung cancer cells. *Oncol. Rep*. 40:2363–2370.

Huang, J., Z. Long, W. Lin, X. Liao, Y. Xie, L. Liu, and W. Ma. 2018b. Integrative omics analysis of p53-dependent regulation of metabolism. *FEBS Lett*. 592:380–393. https://doi.org/10.1002/1873-3468.12968

Huo, H., Z. Zhou, J. Qin, W. Liu, B. Wang, and Y. Gu. 2016. Erastin Disrupts Mitochondrial Permeability Transition Pore (mPTP) and Induces Apoptotic Death of Colorectal Cancer Cells. *PLoS One*. 11. e0154605. https://doi.org/10.1371/journal.pone.0154605

Jacks, T., L. Remington, B.O. Williams, E.M. Schmitt, S. Halachmi, R.T. Bronson, and R.A. Weinberg. 1994. Tumor spectrum analysis in p53-mutant mice. *Curr. Biol*. 4:1–7. https://doi.org/10.1016/S0960-9822(00)00002-6

Jang, C.Y., and G. Fang. 2011. DDA3 associates with MCAK and controls chromosome congression. *Biochem. Biophys. Res. Commun*. 407:610–614. https://doi.org/10.1016/j.bbrc.2011.03.081

Janic, A., L.J. Valente, M.J. Wakefield, L. Di Stefano, L. Milla, S. Wilcox, H. Yang, L. Tai, C.J. Vandenberg, A.J. Kueh, et al. 2018. DNA repair processes are critical mediators of p53-dependent tumor suppression. *Nat. Med*. 24:947–953. https://doi.org/10.1038/s41591-018-0043-5

Jiang, D., C.A. Brady, T.M. Johnson, E.Y. Lee, E.J. Park, M.P. Scott, and L.D. Attardi. 2011. Full p53 transcriptional activation potential is dispensable for tumor suppression in diverse lineages. *Proc. Natl. Acad. Sci. USA*. 108:17123–17128. https://doi.org/10.1073/pnas.1111245108

Jiang, D., E.L. LaGory, D. Kenzelmann Brož, K.T. Bieging, C.A. Brady, N. Link, J.M. Abrams, A.J. Giaccia, and L.D. Attardi. 2015a. Analysis of p53 transactivation domain mutants reveals Acad11 as a metabolic target important for p53 pro-survival function. *Cell Rep*. 10:1096–1109. https://doi.org/10.1016/j.celrep.2015.01.043

Jiang, L., N. Kon, T. Li, S.J. Wang, T. Su, H. Hibshoosh, R. Baer, and W. Gu. 2015b. Ferroptosis as a p53-mediated activity during tumour suppression. *Nature*. 520:57–62. https://doi.org/10.1038/nature14344

Johnson, T.M., E.M. Hammond, A. Giaccia, and L.D. Attardi. 2005. The p53QS transactivation-deficient mutant shows stress-specific apoptotic activity and induces embryonic lethality. *Nat. Genet*. 37:145–152. https://doi.org/10.1038/ng1498

Kaiser, A.M., and L.D. Attardi. 2018. Deconstructing networks of p53-mediated tumor suppression in vivo. *Cell Death Differ*. 25:93–103. https://doi.org/10.1038/cdd.2017.171

Karimian, A., Y. Ahmadi, and B. Yousefi. 2016. Multiple functions of p21 in cell cycle, apoptosis and transcriptional regulation after DNA damage. *DNA Repair (Amst.)*. 42:63–71. https://doi.org/10.1016/j.dnarep.2016.04.008

Kawauchi, K., and S.J. Wolf. 2014. Understanding p53: new insights into tumor suppression. *Expert Rev. Anticancer Ther*. 14:1101–1103. https://doi.org/10.1586/14737140.2014.948859

Kenzelmann Broz, D., S. Spano Mello, K.T. Bieging, D. Jiang, R.L. Dusek, C.A. Brady, A. Sidow, and L.D. Attardi. 2013. Global genomic profiling reveals an extensive p53-regulated autophagy program contributing to key p53 responses. *Genes Dev*. 27:1016–1031. https://doi.org/10.1101/gad.212282.112

Kim, J., Z. Hu, L. Cai, K. Li, E. Choi, B. Faubert, D. Bezwada, J. Rodriguez-Canales, P. Villalobos, Y.F. Lin, et al. 2017. CPS1 maintains pyrimidine pools and DNA synthesis in KRAS/LKB1-mutant lung cancer cells. *Nature*. 546:168–172. https://doi.org/10.1038/nature22359

Krause, M., and A. Gautreau. 2014. Steering cell migration: lamellipodium dynamics and the regulation of directional persistence. *Nat. Rev. Mol. Cell Biol*. 15:577–590. https://doi.org/10.1038/nrm3861

Kuffer, C., A.Y. Kuznetsova, and Z. Storchová. 2013. Abnormal mitosis triggers p53-dependent cell cycle arrest in human tetraploid cells. *Chromosoma*. 122:305–318. https://doi.org/10.1007/s00412-013-0414-0

Kuleshov, M.V., M.R. Jones, A.D. Rouillard, N.F. Fernandez, Q. Duan, Z. Wang, S. Koplev, S.L. Jenkins, K.M. Jagodnik, A. Lachmann, et al. 2016. Enrichr: a comprehensive gene set enrichment analysis web server 2016 update. *Nucleic Acids Res*. 44(W1):W90–W97. https://doi.org/10.1093/nar/gkw377

Lane, D.P.. 1992. Cancer. p53, guardian of the genome. *Nature*. 358:15–16. https://doi.org/10.1038/358015a0

Lanni, J.S., and T. Jacks. 1998. Characterization of the p53-dependent postmitotic checkpoint following spindle disruption. *Mol. Cell. Biol*. 18:1055–1064. https://doi.org/10.1128/MCB.18.2.1055

Lee, K.H., M. Li, A.M. Michalowski, X. Zhang, H. Liao, L. Chen, Y. Xu, X. Wu, and J. Huang. 2010. A genomewide study identifies the Wnt signaling pathway as a major target of p53 in murine embryonic stem cells. *Proc. Natl. Acad. Sci. USA*. 107:69–74. https://doi.org/10.1073/pnas.0909734107

Levine, A.J.. 2018. Reviewing the future of the P53 field. *Cell Death Differ*. 25:1–2. https://doi.org/10.1038/cdd.2017.181

Li, M., Y. He, W. Dubois, X. Wu, J. Shi, and J. Huang. 2012a. Distinct regulatory mechanisms and functions for p53-activated and p53-repressed DNA damage response genes in embryonic stem cells. *Mol. Cell*. 46:30–42. https://doi.org/10.1016/j.molcel.2012.01.020

Li, T., N. Kon, L. Jiang, M. Tan, T. Ludwig, Y. Zhao, R. Baer, and W. Gu. 2012b. Tumor suppression in the absence of p53-mediated cell-cycle arrest, apoptosis, and senescence. *Cell*. 149:1269–1283. https://doi.org/10.1016/j.cell.2012.04.026

Liang, L., J. Guan, Y. Zeng, J. Wang, X. Li, X. Zhang, and Y. Ding. 2011. Down-regulation of formin-like 2 predicts poor prognosis in hepatocellular carcinoma. *Hum. Pathol*. 42:1603–1612. https://doi.org/10.1016/j.humpath.2010.08.025

Lin, A.W., M. Barradas, J.C. Stone, L. van Aelst, M. Serrano, and S.W. Lowe. 1998. Premature senescence involving p53 and p16 is activated in

response to constitutive MEK/MAPK mitogenic signaling. *Genes Dev*. 12: 3008–3019. https://doi.org/10.1101/gad.12.19.3008

Liu, G., J.M. Parant, G. Lang, P. Chau, A. Chavez-Reyes, A.K. El-Naggar, A. Multani, S. Chang, and G. Lozano. 2004. Chromosome stability, in the absence of apoptosis, is critical for suppression of tumorigenesis in Trp53 mutant mice. *Nat. Genet*. 36:63–68. https://doi.org/10.1038/ng1282

Lowe, S.W., T. Jacks, D.E. Housman, and H.E. Ruley. 1994. Abrogation of oncogene-associated apoptosis allows transformation of p53-deficient cells. *Proc. Natl. Acad. Sci. USA*. 91:2026–2030. https://doi.org/10.1073/pnas.91.6.2026

Love, M.I., W. Huber, and S. Anders. 2014. Moderated estimation of fold change and dispersion for RNA-seq data with DESeq2. *Genome Biology*. 15:550. https://doi.org/10.1186/s13059-014-0550-8

Lowe, S.W., H.E. Ruley, T. Jacks, and D.E. Housman. 1993. p53-dependent apoptosis modulates the cytotoxicity of anticancer agents. *Cell*. 74: 957–967. https://doi.org/10.1016/0092-8674(93)90719-7

Maddocks, O.D., C.R. Berkers, S.M. Mason, L. Zheng, K. Blyth, E. Gottlieb, and K.H. Vousden. 2013. Serine starvation induces stress and p53-dependent metabolic remodelling in cancer cells. *Nature*. 493:542–546. https://doi.org/10.1038/nature11743

McDade, S.S., D. Patel, M. Moran, J. Campbell, K. Fenwick, I. Kozarewa, N.J. Orr, C.J. Lord, A.A. Ashworth, and D.J. McCance. 2014. Genome-wide characterization reveals complex interplay between TP53 and TP63 in response to genotoxic stress. *Nucleic Acids Res*. 42:6270–6285. https://doi.org/10.1093/nar/gku299

Mello, S.S., and L.D. Attardi. 2018. Deciphering p53 signaling in tumor suppression. *Curr. Opin. Cell Biol*. 51:65–72. https://doi.org/10.1016/j.ceb.2017.11.005

Menendez, D., T.A. Nguyen, J.M. Freudenberg, V.J. Mathew, C.W. Anderson, R. Jothi, and M.A. Resnick. 2013. Diverse stresses dramatically alter genome-wide p53 binding and transactivation landscape in human cancer cells. *Nucleic Acids Res*. 41:7286–7301. https://doi.org/10.1093/nar/gkt504

Michalak, E.M., E.S. Jansen, L. Happo, M.S. Cragg, L. Tai, G.K. Smyth, A. Strasser, J.M. Adams, and C.L. Scott. 2009. Puma and to a lesser extent Noxa are suppressors of Myc-induced lymphomagenesis. *Cell Death Differ*. 16:684–696. https://doi.org/10.1038/cdd.2008.195

Mullen, A.R., Z. Hu, X. Shi, L. Jiang, L.K. Boroughs, Z. Kovacs, R. Boriack, D. Rakheja, L.B. Sullivan, W.M. Linehan, et al. 2014. Oxidation of alpha-ketoglutarate is required for reductive carboxylation in cancer cells with mitochondrial defects. *Cell Rep*. 7:1679–1690. https://doi.org/10.1016/j.celrep.2014.04.037

Muller, P.A., K.H. Vousden, and J.C. Norman. 2011. p53 and its mutants in tumor cell migration and invasion. *J. Cell Biol*. 192:209–218. https://doi.org/10.1083/jcb.201009059

Narita, M., S. Nunez, E. Heard, M. Narita, A.W. Lin, S.A. Hearn, D.L. Spector, G.J. Hannon, and S.W. Lowe. 2003. Rb-mediated heterochromatin formation and silencing of E2F target genes during cellular senescence. *Cell*. 113:703–716. https://doi.org/10.1016/S0092-8674(03)00401-X

Nikulenkov, F., C. Spinnler, H. Li, C. Tonelli, Y. Shi, M. Turunen, T. Kivioja, I. Ignatiev, A. Kel, J. Taipale, et al. 2012. Insights into p53 transcriptional function via genome-wide chromatin occupancy and gene expression analysis. *Cell Death Differ*. 19:1992–2002. https://doi.org/10.1038/cdd.2012.89

Parrinello, S., E. Samper, A. Krtolica, J. Goldstein, S. Melov, and J. Campisi. 2003. Oxygen sensitivity severely limits the replicative lifespan of murine fibroblasts. *Nat. Cell Biol*. 5:741–747. https://doi.org/10.1038/ncb1024

Pollard, T.D., and J.A. Cooper. 2009. Actin, a central player in cell shape and movement. *Science*. 326:1208–1212. https://doi.org/10.1126/science.1175862

Rai, A.K., J.X. Chen, M. Selbach, and L. Pelkmans. 2018. Kinase-controlled phase transition of membraneless organelles in mitosis. *Nature*. 559: 211–216. https://doi.org/10.1038/s41586-018-0279-8

Sakaue-Sawano, A., H. Kurokawa, T. Morimura, A. Hanyu, H. Hama, H. Osawa, S. Kashiwagi, K. Fukami, T. Miyata, H. Miyoshi, et al. 2008. Visualizing spatiotemporal dynamics of multicellular cell-cycle progression. *Cell*. 132:487–498. https://doi.org/10.1016/j.cell.2007.12.033

Schwenk, F., U. Baron, and K. Rajewsky. 1995. A cre-transgenic mouse strain for the ubiquitous deletion of loxP-flanked gene segments including deletion in germ cells. *Nucleic Acids Res*. 23:5080–5081. https://doi.org/10.1093/nar/23.24.5080

Soengas, M.S., R.M. Alarcón, H. Yoshida, A.J. Giaccia, R. Hakem, T.W. Mak, and S.W. Lowe. 1999. Apaf-1 and caspase-9 in p53-dependent apoptosis and tumor inhibition. *Science*. 284:156–159. https://doi.org/10.1126/science.284.5411.156

Stelzer, G., N. Rosen, I. Plaschkes, S. Zimmerman, M. Twik, S. Fishilevich, T.I. Stein, R. Nudel, I. Lieder, Y. Mazor, et al. 2016. The GeneCards Suite: From Gene Data Mining to Disease Genome Sequence Analyses. *Curr. Protoc. Bioinformatics*. 54:1.30.1-1.30.33. https://doi.org/10.1002/cpbi.5

Stevenson, R.P., D. Veltman, and L.M. Machesky. 2012. Actin-bundling proteins in cancer progression at a glance. *J. Cell Sci*. 125:1073–1079. https://doi.org/10.1242/jcs.093799

Stockwell, B.R., J.P. Friedmann Angeli, H. Bayir, A.I. Bush, M. Conrad, S.J. Dixon, S. Fulda, S. Gascón, S.K. Hatzios, V.E. Kagan, et al. 2017. Ferroptosis: A Regulated Cell Death Nexus Linking Metabolism, Redox Biology, and Disease. *Cell*. 171:273–285. https://doi.org/10.1016/j.cell.2017.09.021

Tanikawa, C., Y.Z. Zhang, R. Yamamoto, Y. Tsuda, M. Tanaka, Y. Funauchi, J. Mori, S. Imoto, R. Yamaguchi, Y. Nakamura, et al. 2017. The Transcriptional Landscape of p53 Signalling Pathway. *EBioMedicine*. 20: 109–119. https://doi.org/10.1016/j.ebiom.2017.05.017

Tavares, S., A.F. Vieira, A.V. Taubenberger, M. Araújo, N.P. Martins, C. Brás-Pereira, A. Polónia, M. Herbig, C. Barreto, O. Otto, et al. 2017. Actin stress fiber organization promotes cell stiffening and proliferation of pre-invasive breast cancer cells. *Nat. Commun*. 8:15237. https://doi.org/10.1038/ncomms15237

Tojkander, S., G. Gateva, and P. Lappalainen. 2012. Actin stress fibers--assembly, dynamics and biological roles. *J. Cell Sci*. 125:1855–1864. https://doi.org/10.1242/jcs.098087

Tonelli, C., M.J. Morelli, S. Bianchi, L. Rotta, T. Capra, A. Sabò, S. Campaner, and B. Amati. 2015. Genome-wide analysis of p53 transcriptional programs in B cells upon exposure to genotoxic stress in vivo. *Oncotarget*. 6: 24611–24626. https://doi.org/10.18632/oncotarget.5232

Tyner, S.D., J. Choi, R. Laucirica, R.J. Ford, and L.A. Donehower. 1999. Increased tumor cell proliferation in murine tumors with decreasing dosage of wild-type p53. *Mol. Carcinog*. 24:197–208. https://doi.org/10.1002/(SICI)1098-2744(199903)24:3<197::AID-MC6>3.0.CO;2-V

Valente, L.J., D.H. Gray, E.M. Michalak, J. Pinon-Hofbauer, A. Egle, C.L. Scott, A. Janic, and A. Strasser. 2013. p53 efficiently suppresses tumor development in the complete absence of its cell-cycle inhibitory and proapoptotic effectors p21, Puma, and Noxa. *Cell Rep*. 3:1339–1345. https://doi.org/10.1016/j.celrep.2013.04.012

Vousden, K.H., and C. Prives. 2009. Blinded by the Light: The Growing Complexity of p53. *Cell*. 137:413–431. https://doi.org/10.1016/j.cell.2009.04.037

Vousden, K.H., and K.M. Ryan. 2009. p53 and metabolism. *Nat. Rev. Cancer*. 9: 691–700. https://doi.org/10.1038/nrc2715

Wang, B., D. Niu, T.H. Lam, Z. Xiao, and E.C. Ren. 2014. Mapping the p53 transcriptome universe using p53 natural polymorphs. *Cell Death Differ*. 21:521–532. https://doi.org/10.1038/cdd.2013.132

Williams, A.B., and B. Schumacher. 2016. p53 in the DNA-Damage-Repair Process. *Cold Spring Harb. Perspect. Med*. 6. a026070. https://doi.org/10.1101/cshperspect.a026070

Yin, C., C.M. Knudson, S.J. Korsmeyer, and T. Van Dyke. 1997. Bax suppresses tumorigenesis and stimulates apoptosis in vivo. *Nature*. 385:637–640. https://doi.org/10.1038/385637a0

JCB

Supplemental material

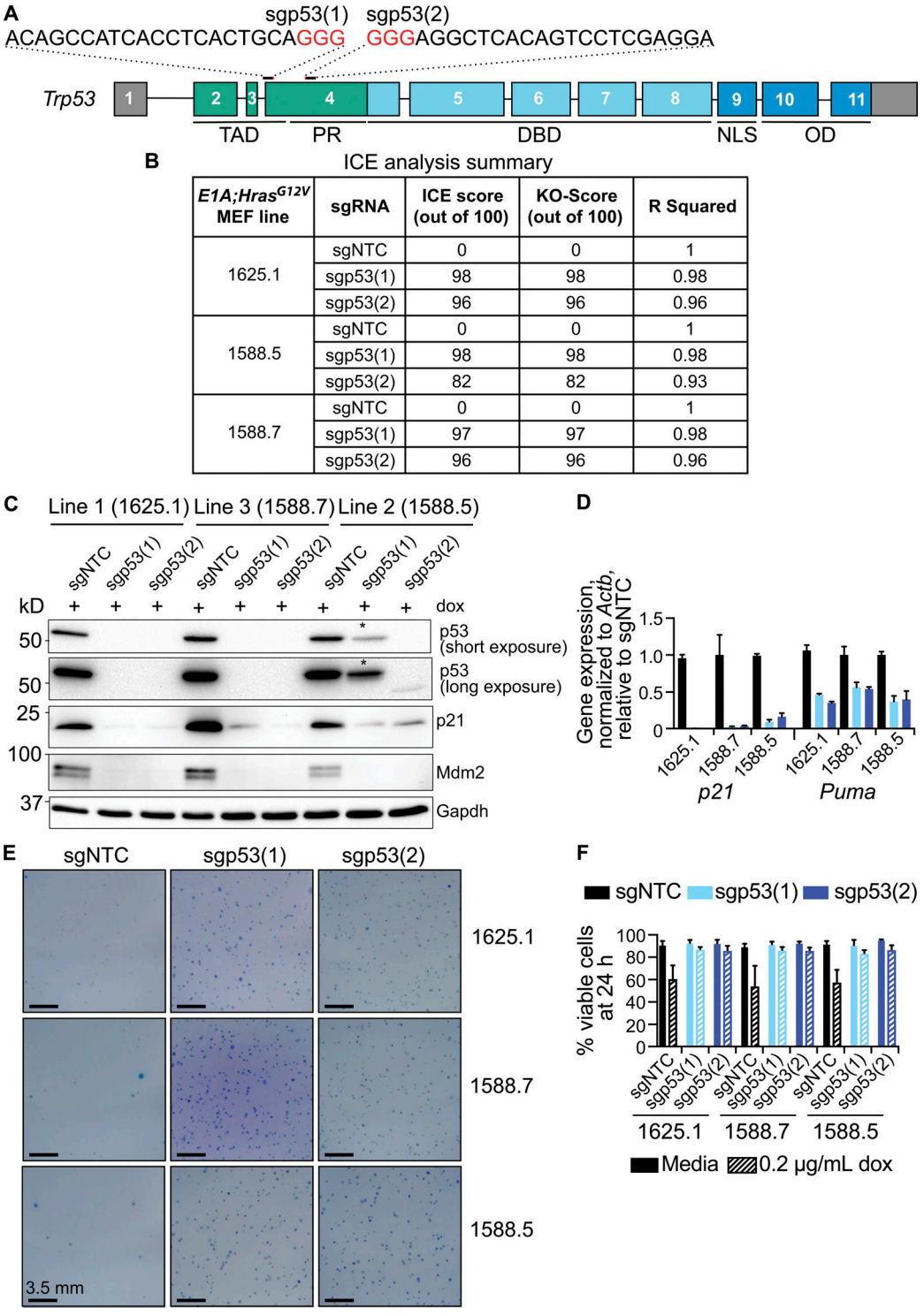

E1A;Hras^{G12V} MEF line	sgRNA	ICE score (out of 100)	KO-Score (out of 100)	R Squared
1625.1	sgNTC	0	0	1
	sgp53(1)	98	98	0.98
	sgp53(2)	96	96	0.96
1588.5	sgNTC	0	0	1
	sgp53(1)	98	98	0.98
	sgp53(2)	82	82	0.93
1588.7	sgNTC	0	0	1
	sgp53(1)	97	97	0.98
	sgp53(2)	96	96	0.96

Figure S1. **Generation and validation of isogenic, WT, and *p53*-null *E1A;Hras*^{G12V};*H11*^{Cas9} MEFs. (A)** *Trp53* exon structure and the binding sequences of the two sgRNAs used to target *p53* in this study. PAM motifs are in red. Exons encoding different p53 domains are also indicated: transactivation domain (TAD), proline rich domain (PR), DNA binding domain (DBD), nuclear localization signal (NLS), and oligomerization domain (OD). **(B)** Summary of ICE analysis on *E1A;Hras*^{G12V};*H11*^{Cas9} MEFs used in this study. ICE score represents the percentage of sequences within the pool with non–WT sequences, whereas the KO score represents the percentage of sequences in the pool with either a frameshift or 21+-bp indel. R squared values refer to the Pearson correlation coefficient for the ICE score. **(C)** Western blot analysis of p53, p21, and Mdm2 after doxorubicin (dox) treatment of all nine *E1A;Hras*^{G12V} MEF lines used in this study. Gapdh serves as a loading control. **(D)** qRT-PCR analysis of p53 target gene expression in all nine *E1A;Hras*^{G12V} MEF lines used in this study. *n* = 3 cell lines/sgRNA (in triplicate). Data are presented as mean ± SD, after normalization to β-actin. **(E)** Representative images of soft agar assays of all nine sgRNA-targeted *E1A;Hras*^{G12V} MEF lines used in study. *n* = 3 cell lines/sgRNA. Scale bar, 3.5 mm. **(F)** Cell viability analysis (AnnexinV, PI-negative cells) on all sgRNA-targeted *E1A;Hras*^{G12V} MEFs 24 h after DNA damage (doxorubicin treatment). *n* = 3 cell lines/sgRNA, three to five independent experiments. Data are presented as mean ± SD. For A–F, all experiments were performed in 5% O_2.

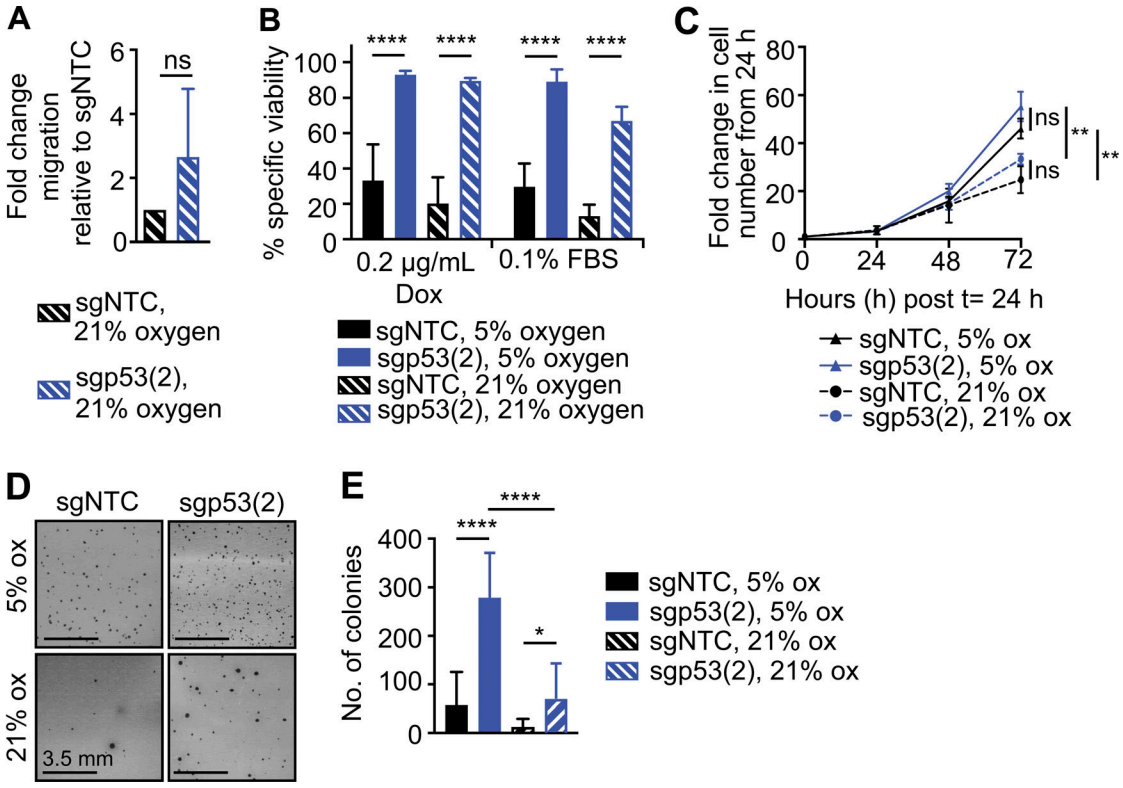

Figure S2. **The impact of physiological (5%) and atmospheric (21%) oxygen tension on cell behavior in vitro. (A)** Analysis of migration in *E1A;Hras*^{G12V} MEFs in 21% O_2. Data are mean fold change in migrating cells ± SD, expressed relative to counterpart sgNTC control cell line. *n* = 3 cell lines/sgRNA; ns, not significant (P > 0.05), Mann–Whitney unpaired *t* test. **(B)** Cell viability analysis by AnnexinV/PI staining of sgNTC and sgp53(2) *E1A;Hras*^{G12V} MEFs in 5% or 21% O_2 cotreated with 0.2 µg/ml doxorubicin or 0.1% FBS for 24 h. *n* = 3 independent experiments for each sgRNA. Data are presented as mean ± SD; ****, P < 0.0001; ns, not significant (P > 0.05), two-way ANOVA, Sidak's multiple comparison posttest. **(C)** Proliferation of *E1A;Hras*^{G12V} MEFs in 5% or 21% O_2 measured by cell counting starting 24 h after plating. *n* = 3 cell lines/sgRNA. Data are mean fold change in cell number ± SD; **, P < 0.005; not significant (P > 0.05), linear regression analysis. **(D)** Representative soft agar assays measuring anchorage-independent growth of sgNTC and sgp53(2)-targeted *E1A;Hras*^{G12V} MEFs in 5% or 21% O_2. Scale bar, 3.5 mm. **(E)** Average colony number ± SD of sgNTC and sgp53(2) *E1A;Hras*^{G12V} MEFs in 5% and 21% O_2. *n* = 3 cell lines/sgRNA, in triplicate; *, P < 0.05; ****, P < 0.0001; ns, not significant (P > 0.05), one-way ANOVA, Tukey's multiple comparison posttest.

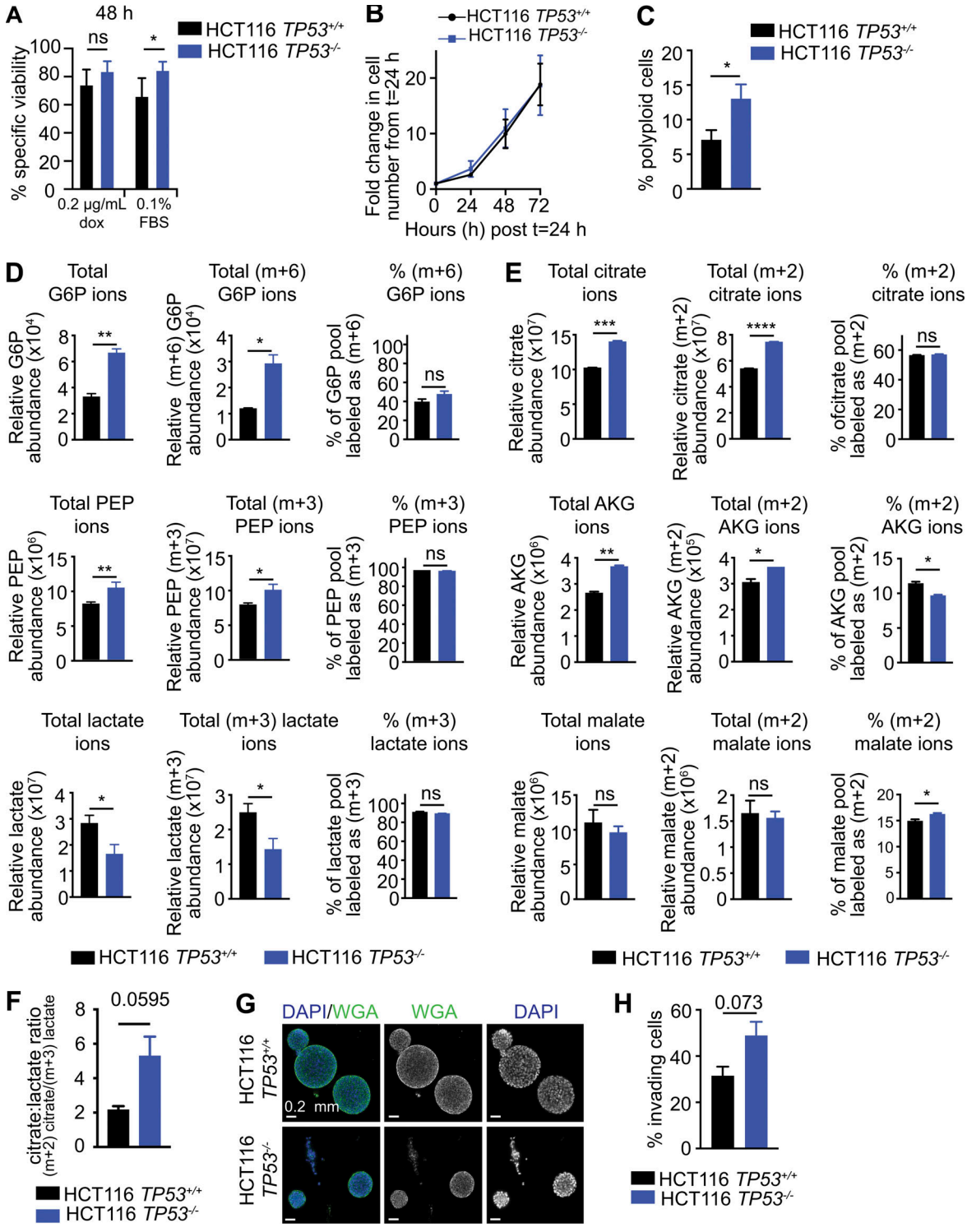

Figure S3. **Loss of p53 in human HCT116 colon carcinoma cells alters the behavior of multiple cellular pathways. (A)** Cell viability analysis by AnnexinV/PI staining on *TP53*$^{+/+}$ and *TP53*$^{-/-}$ HCT116 cells in 5% O_2 after 0.2 µg/ml doxorubicin or 0.1% FBS treatment for 48 h. *n* = 3 independent experiments for each genotype. Data are presented as mean ± SD; *, P < 0.05, two-way ANOVA, Sidak's multiple comparison posttest. **(B)** Proliferation analysis of *TP53*$^{+/+}$ and *TP53*$^{-/-}$ HCT116 cells measured by cell counting starting 24 h after plating. *n* = 3 independent experiments. Data are presented as mean fold change in cell number ± SD. **(C)** Ploidy analysis in *TP53*$^{+/+}$ and *TP53*$^{-/-}$ HCT116 cells showing percentage of cells with >4N DNA content by PI staining. *n* = 3 independent experiments per genotype; data represent mean ± SD; *, P < 0.05, unpaired *t* test. **(D and E)** [U^{13}C]glucose tracing on *TP53*$^{+/+}$ and *TP53*$^{-/-}$ HCT116 cells showing glycolytic (D) and TCA cycle (E) intermediates. Data represent mean ± SD of *n* = 3 cell lines per sgRNA; *, P < 0.05; **, P > 0.005; ***, P < 0.001; ****, P < 0.0001, one-way ANOVA, Tukey's multiple comparison test. **(F)** Citrate:lactate mass heavy ion ratio of *TP53*$^{+/+}$ and *TP53*$^{-/-}$ HCT116 cells. Data represent mean ± SD of *n* = 2 samples per cell line; Student's *t* test. **(G)** Representative images of *TP53*$^{+/+}$ and *TP53*$^{-/-}$ HCT116 cells grown in a 3D collagen matrix. WGA stains cell membranes, and DAPI marks nuclei. Scale bar, 0.2 mm. **(H)** Percentage of invading colonies in 3D collagen assay. Data are mean ± SD, *n* = 2 independent experiments per genotype, P = 0.073, unpaired *t* test. All HCT116 experiments were performed in 5% O_2.

	Mouse									Human						
	RNA-seq						ChIP-seq			RNA-seq			ChIP-seq			
	In vitro					*In vivo*	*In vitro*			*In vitro*			*In vitro*			
Study	**Current**	Tonelli *et al.*, 2015	Kenzelmann Broz *et al.*, 2013	Lee *et al.*, 2010	Li *et al.*, 2012a	Tanikawa, 2017	Kenzelmann Broz *et al.*, 2013	Lee *et al.*, 2010	Li *et al.*, 2012a	Wang *et al.*, 2014	Nikulenkov *et al.*, 2012	Allen *et al.*, 2014*	Wang *et al.*, 2014	Nikulenkov *et al.*, 2012	Menendez *et al.*, 2013	McDade *et al.*, 2014
RhoD	**UP**	UP	UP	UP	UP	UP	BOUND	BOUND	BOUND		UP	UP		BOUND		BOUND
RhoV	**UP**		UP			UP	BOUND							BOUND		
RhoE	**DOWN**				DOWN				BOUND	UP			BOUND	BOUND	BOUND	

Figure S4. **Meta-analysis of p53 binding and p53-dependent RhoGTPase expression in human and mouse RNA-seq and ChIP-seq datasets.** Meta-analysis of *RhoD*, *RhoV*, and *RhoE* in published in vitro and in vivo mouse and human RNA-seq and ChIP-seq datasets examining p53 binding and p53-regulated expression. UP/DOWN indicates gene expression was enriched/repressed relative to controls; BOUND indicates p53-binding peaks. Gray boxes refer to studies in which the gene was not found.

Video 1. **Time-lapse live imaging of sgNTC- and sgp53-targeted *E1A;Hras^{G12V};H11^{Cas9}* MEFs undergoing normal and abnormal mitosis.** Normal and abnormal mitoses in sgNTC and sgp53(2)-targeted *E1A;HRas^{G12V}* MEFs. 16-h phase-contrast live imaging, image capture every 5 min, frame rate = 5 frames/s.

Video 2. **Time-lapse live imaging of sgNTC- and sgp53-targeted *E1A;Hras^{G12V};H11^{Cas9}* MEFs migrating in 2D.** Cell migration in 2D of sgNTC and sgp53(2)-targeted *E1A;Hras^{G12V}* MEFs. 16 h frames/s.

Two tables are provided online in Excel files. Table S1 shows the metabolomics dataset: sgNTC- and sgp53(2)-targeted *E1A;Hras^{G12V}* MEFs grown in 5% O_2 for 24 h. Table S2 shows the RNA-seq dataset from *E1A;Hras^{G12V}* MEFs in 5% O_2, annotated to show genes that had p53 ChIP peaks in the Kenzelmann Broz et al. (2013) ChIP seq dataset.